A two-scale Stefan problem arising in a model for tree sap exudation

ISABELL KONRAD

*Department of Mathematics, Simon Fraser University, 8888 University Drive, Burnaby, BC,
V5A 1S6, Canada*
isabella.konrad@gmail.com

MALTE A. PETER

*Institut für Mathematik, University of Augsburg, Universitätsstraße 14, 86159 Augsburg,
Germany and Augsburg Centre for Innovative Technologies, University of Augsburg, 86135
Augsburg, Germany*
malte.peter@math.uni-augsburg.de

AND

JOHN M. STOCKIE

*Department of Mathematics, Simon Fraser University, 8888 University Drive, Burnaby, BC,
V5A 1S6, Canada*
Corresponding author: stockie@math.sfu.ca

The study of tree sap exudation, in which a (leafless) tree generates elevated stem pressure in response to repeated daily freeze–thaw cycles, gives rise to an interesting multiscale problem involving heat and multiphase liquid/gas transport. The pressure generation mechanism is a cellular-level process that is governed by differential equations for sap transport through porous cell membranes, phase change, heat transport, and generation of osmotic pressure. By assuming a periodic cellular structure based on an appropriate reference cell, we derive an homogenized heat equation governing the global temperature on the scale of the tree stem, with all the remaining physics relegated to equations defined on the reference cell. We derive a corresponding strong formulation of the limit problem and use it to design an efficient numerical solution algorithm. Numerical simulations are then performed to validate the results and draw conclusions regarding the phenomenon of sap exudation, which is of great importance in trees such as sugar maple and a few other related species. The particular form of our homogenized temperature equation is obtained using periodic homogenization techniques with two-scale convergence, which we investigate theoretically in the context of a simpler two-phase Stefan-type problem corresponding to a periodic array of melting cylindrical ice bars with a constant thermal diffusion coefficient. For this reduced model, we prove results on existence, uniqueness and convergence of the two-scale limit solution in the weak form, clearly identifying the missing pieces required to extend the proofs to the fully nonlinear sap exudation model. Numerical simulations of the reduced equations are then compared with results from the complete sap exudation model.

Keywords: periodic homogenization; two-scale convergence; Stefan problem; multiphase flow; phase change.

MSC(2010): 35B27, 35R37, 76T30, 80A22, 92C80.

1. Introduction

This paper is motivated by the study of sap flow in sugar maple trees that are subject to repeated cycles of thawing and freezing during the sap harvest season in late winter (Ceseri & Stockie, 2013). We seek insight into the phenomenon of *sap exudation*, which refers to the generation of elevated sap pressure within the maple stem when the tree is in a leafless state and no transpiration occurs to drive the sap flow. Our work is based on the model derived in Ceseri & Stockie (2013) that captures the physical processes at the microscale (i.e., at the level of individual wood cells) and includes multiphase flow of ice/water/gas, heat transport, porous flow through cell walls, and osmosis. There is an inherent repeating structure in sapwood at the cellular scale that lends itself naturally to the use of homogenization ideas that we exploited in Graf et al. (2015) to obtain a multiscale model for the macroscale temperature that is coupled to a corresponding system of equations governing the microscale cellular processes. Our main objective in this paper is to provide a more rigorous theoretical justification for this multiscale model by working through the details of the homogenization process and proving results regarding existence, uniqueness and two-scale convergence.

Multiscale problems such as the one just described are characterized by geometric, material or other features that exhibit variations on widely differing spatial scales. Many mathematical and numerical methods have been developed to capture such scale separation as well as the interactions between physical phenomena operating on disparate scales (Engquist et al., 2005; Hornung, 1997). For problems having a periodic microstructure, a mathematical technique that has proven to be very effective is known as periodic homogenization (Cioranescu & Donato, 1999), and more specifically the method of two-scale convergence (Allaire, 1992; Nguetseng, 1989), which has also been extended to capture non-periodically evolving microstructures (Peter, 2007a,b; Peter & Böhm, 2009). We are interested here in applying two-scale convergence to analyze solutions of a Stefan-type problem that governs the dynamics of the ice/water interface within individual tree cells. Locally, temperature obeys the heat equation and is coupled with a Stefan condition that governs solid–liquid phase transitions at the interface. Many different approaches have been developed to analyze such phase transitions, which are well-described in Visintin (1996). With the exception of a few studies of (single-phase) water and solute transport in plant tissues (Chavarría-Krauser & Ptashnyk, 2010; Chavarría-Krauser & Ptashnyk, 2013), periodic homogenization techniques have not been applied in the context of heat or sap flow in trees.

The approach we employ in this paper has the advantage that it applies homogenization techniques in a straightforward manner in order to obtain an uncomplicated limit model, the simplicity of which ensures that numerical simulations are relatively easy to perform. In particular, we define a reference cell Y that is divided into two sub-regions: Y^1, where the temperature diffuses rapidly; and Y^2, on which we define a second temperature field that diffuses slowly. Refer to Arbogast et al. (1990) and Peter & Böhm (2008) for similar homogenization approaches involving slow and fast transport. One particular challenge arising in the study of Stefan problems is that the diffusion coefficient depends on the underlying phases, so that heat diffuses differently in water or ice. Consequently, the diffusion coefficient depends on temperature (or equivalently on enthalpy) so that the governing differential equation is only quasi-linear.

Rather than attempting to analyze the sap exudation problem in its full complexity, we find it more convenient to develop our homogenization results in the context of a simpler "reduced model" defined on a similarly fine-structured domain wherein the cell-level processes are governed by a Stefan problem that involves only heat transport and ice/water phase change. In particular, we consider a domain consisting of a periodic array of cylindrical ice inclusions immersed in water. To handle the multiplicity of the ice bars, we apply the technique of periodic homogenization with two-scale convergence established in

Allaire (1992) and Nguetseng (1989). Several authors have previously applied homogenization to Stefan problems, such as Bossavit & Damlamian (1981), Damlamian (1981) and Visintin (2007), where the phase change boundary is handled by separately homogenizing an auxiliary problem. In Eck (2004) on the other hand, an additional function θ is introduced for an aggregate state that diffuses on a slow time scale and with which all microscopic phase changes are properly captured. When we show existence for the heat equation with phase transitions, we deduce a general existence result for quasi-linear parabolic differential equations having a non-monotone nonlinearity in the diffusion operator, which is of general interest in the context of heat transport and Stefan problems (even in a single-scale setting).

This paper is organized as follows. We begin in Section 2 by providing background material on the physics of maple sap exudation, along with a description of the governing equations at the cellular level. A reduced model involving only melting of ice is introduced in Section 3 for the purposes of more easily deriving the two-scale convergence results. The main analytical results on existence, a priori estimates, two-scale convergence and uniqueness are presented in Section 4, and detailed proofs of the key results are relegated to the Appendix. Following that, we state in Section 4.7 the strong form of the limit problem for the reduced model, which in turn suggests a corresponding strong form of the original sap exudation model in Section 4.8. These limit problems lead naturally to a multiscale numerical algorithm that is described in Section 5, after which numerical simulations of both problems are presented and compared.

2. Mathematical model for sap exudation

Before presenting the details of the mathematical model, it is necessary to introduce some background material on the phenomenon of sap exudation. Sugar maple trees (along with a few related species such as red or black maple, black walnut, and birch) have a unique ability compared to other deciduous tree species in that they exude large quantities of sap during the winter when they are in a leafless state. Sap exudation originates from an elevated pressure in the tree stem that is generated over a period of several days during which the air temperature oscillates above and below the freezing point. The ability of maple to exude sap has intrigued tree physiologists for over a century, and various physical and biological processes have been proposed to explain this behaviour (Johnson et al., 1987; Milburn & Kallarackal, 1991; Tyree, 1995). Until recently, a significant degree of controversy existed over the root causes of sap exudation, and the most plausible and widely-accepted explanation has been a freeze–thaw hypothesis proposed by Milburn & O'Malley (1984). This hypothesis forms the basis of the mathematical model for the cellular processes underlying exudation during a thawing event that was developed by Ceseri & Stockie (2013), which was subsequently extended to capture a complete freeze–thaw cycle by Graf et al. (2015).

2.1 *Background: Tree physiology and the Milburn–O'Malley process*

The Milburn–O'Malley process depends crucially on the distinctive microstructure of sapwood (or xylem) in sugar maple trees (*Acer saccharum*). Wood in most deciduous tree species consists of roughly cylindrical cells that are on the order of 1 mm in length. These cells can be classified into two main types: *vessels* having an average radius of 20 μm, which are surrounded by the much more numerous *(libriform) fibers* with a radius of approximately 3–4 μm. The repeating structure of vessels and fibers is illustrated in Figure 1a. The vessels have a significantly larger diameter and therefore comprise the main route for sap transport between roots to leaves during the growing season, whereas the fibers are understood to play a largely passive and more structural role. Under normal conditions the vessels are filled

with sap, which is composed primarily of water but also contains as much as 2–5% sugar by weight in species like *Acer*. On the other hand, the fibers are thought to be primarily filled with gas (i.e., air). We note that experiments exhibit small but measurable amounts of gas also being present within the vessel sap, either as bubbles or in dissolved form.

(a) Sapwood microstructure
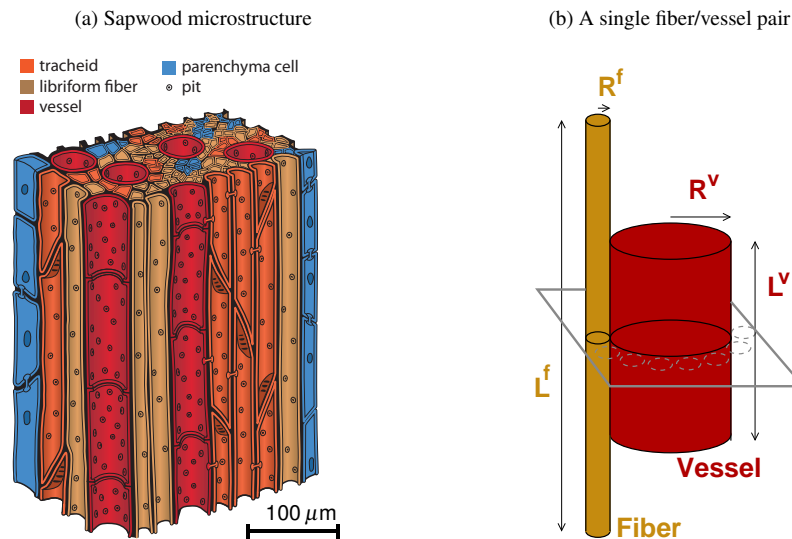
(b) A single fiber/vessel pair

Figure 1. (a) A cut-away view of the sapwood (or xylem) in hardwood trees such as sugar maple, depicting the repeating microstructure of vessels surrounded by fibers (the other cell types indicated here are ignored in our model). (b) A vessel surrounded by N^f fibers, all depicted as circular cylinders (for simplicity, only one fiber is shown). Typical dimensions of the fiber are length $L^f = 1.0 \times 10^{-3}$ m and radius $R^f = 3.5 \times 10^{-6}$ m, whereas the vessel has $L^v = 5.0 \times 10^{-4}$ m and $R^v = 2.0 \times 10^{-5}$ m. The 2D model reference cell introduced in what follows is based on a horizontal cross-section through the middle of the fiber and vessel.

Milburn and O'Malley hypothesized that during late winter when daily high temperatures peak above the freezing point, and just as evening temperatures begin to drop below zero, sap is drawn through tiny pores in the fiber/vessel walls by capillary and adsorption forces into the gas-filled fibers where it forms ice crystals on the inner surface of the fiber wall (top "cooling sequence" in Figure 2). As temperatures drop further, the ice layer grows and the gas trapped inside the fiber is compressed, forming a pressure reservoir of sorts. When temperatures rise above freezing again the next day, the process reverses, with the ice layer melting and the pressurized gas driving liquid melt-water back into the vessel where it then (re-)pressurizes the vessel compartment (bottom "warming sequence" in Figure 2). Milburn and O'Malley also stressed the importance of osmotic pressure in terms of maintaining the high stem pressures actually observed in sugar maple trees. This essential role of osmosis has since been verified experimentally by Cirelli et al. (2008) who confirmed the existence of osmotic pressure arising from a selectively permeable membrane within the fiber/vessel wall. They showed that the cell wall permits water to pass but prevents larger sugar molecules contained in the vessel sap from entering the fiber, thereby introducing a significant osmotic pressure difference between the sugar-rich vessel sap and the pure water contained in the fiber.

There are two additional physical effects not explicitly addressed by Milburn & O'Malley (1984) that are essential in order to obtain physically-consistent results for the sap thawing process. First of all, Ceseri & Stockie (2013) demonstrated the necessity for including gas bubbles suspended within the vessel sap that permit an exchange of pressure between the vessel and fiber compartments, which would
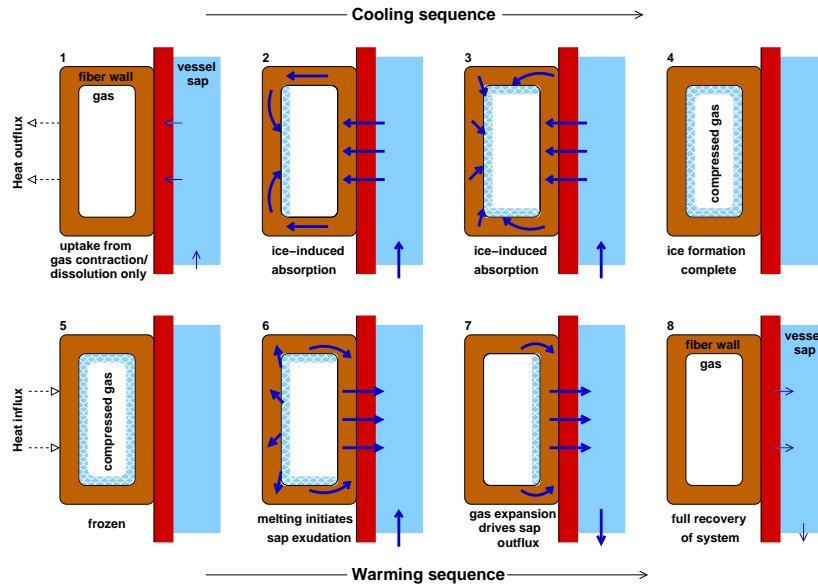
Figure 2. Illustration of the Milburn–O'Malley process in a single fiber/vessel pair (adapted from Milburn & O'Malley (1984, Fig. 7)). We focus on the "warming sequence" in the bottom row, numbered 5–8. The fiber is the large rectangular structure on the left of each sub-image, and the vessel is the vertical channel on the right (not drawn to scale).

otherwise not be possible owing to the incompressibility of water. Secondly, despite the pervading belief that there is no significant root pressure in maple during winter (Kramer & Boyer, 1995; Wilmot, 2011), we found to the contrary that including uptake of root water during the freezing process is absolutely essential in order that pressure can accumulate over multiple freeze–thaw cycles (Graf et al., 2015). Indeed, the need to include root pressure is confirmed by recent experiments (Brown, 2015) that demonstrate the existence of root pressure in maple trees during the sap harvest season.

2.2   *Microscale model for cell-level processes*

The modified Milburn–O'Malley description just presented (with the exception of root pressure) was employed by Ceseri & Stockie (2013) and Graf et al. (2015) to derive a mathematical model for cell-level processes governing sap exudation during a thawing cycle. In this study, we study the same problem, including the effect of the gas phase in both cell chambers (fiber and vessel), but we will assume for the sake of simplicity that the effects of gas dissolution and nucleation are negligible. This is the primary difference between our microscale model and that in Ceseri & Stockie (2013) and Graf et al. (2015), on which it is based. Neglecting root pressure is a reasonable simplification because we are only interested here in studying a single thawing event and not capturing repeated freeze–thaw cycles.

With the above assumptions in mind, we approximate the sapwood as a periodic array of square reference cells Y pictured in Figure 3a. Each reference cell contains a circular fiber of radius R^f located at the centre, surrounded by a vessel compartment that makes up the remainder of the cell. Because the vessels have considerably larger diameter, we assume that on the scale of a fiber the cylindrical geometry of the vessel can be neglected as long as we ensure that appropriate conservation principles (for mass and energy) are maintained within the vessel. This choice of reference cell is obviously

a mathematical idealization that may influence fine details of vessel transport on the microscale but ultimately has minimal impact on the homogenized solution.

The fiber compartment is sub-divided into nested annular regions containing gas, ice and liquid, and the outer radii of the phase interfaces are denoted s_{gi} (for gas/ice) and s_{iw} (for ice/water). The vessel contains a circular gas bubble of radius r which has no specified location but rather is included simply to track the amount of gas for mass-conservation purposes. One additional variable U is introduced to measure the total volume of water transferred from fiber to vessel. The region lying outside the fiber and inside the boundary of Y represents the sugary sap-filled vessel. Note that during a thawing cycle, we are only concerned with a vessel containing liquid sap (no ice) because of the effect of freezing point depression, which ensures that any given vessel thaws before the adjacent fiber(s). This reference cell geometry should be contrasted with that depicted in Ceseri & Stockie (2013, Fig. 3.1).
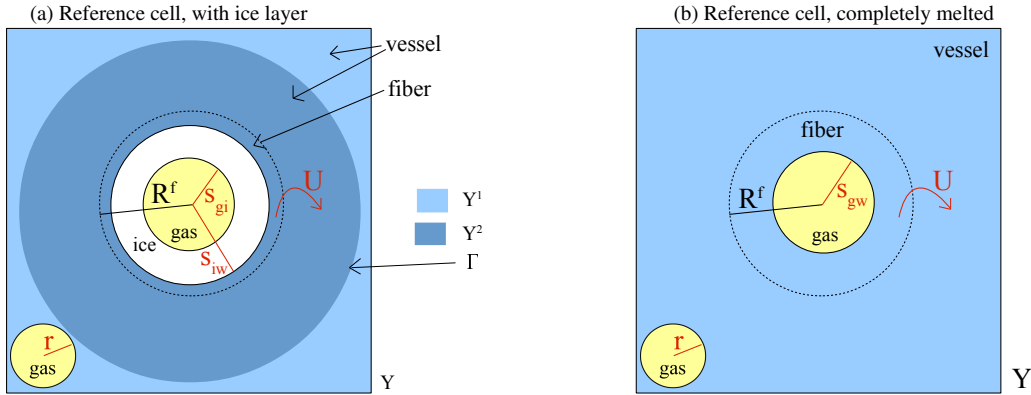

Figure 3. Geometry of the reference cell, Y. (a) For the sap exudation problem, the vessel compartment contains a gas bubble with radius r, while the circular fiber (radius R^f) contains a gas bubble (radius s_{gi}), surrounded by an ice layer (with thickness $s_{iw} - s_{gi}$), and finally a layer of melt-water (with thickness $R^f - s_{iw}$). The porous wall between fiber and vessel is denoted by a dotted line. As ice melts, the melt-water is forced out by gas pressure through the porous fiber wall into the surrounding vessel compartment. The total volume of melt-water transferred from fiber to vessel is denoted U. An artificial boundary Γ is introduced in the homogenization process to differentiate between a region Y^1 (outside Γ) on which thermal diffusion is fast, and Y^2 (inside Γ) on which diffusion is slow. (b) After the ice has completely melted there remains only a gas/water interface, s_{gw}, and a single temperature field can be used to describe the entire reference cell domain $Y \equiv Y^1$.

For the moment, we will consider the four solution variables s_{iw}, s_{gi}, r, U as depending on time t only, with an additional dependence of temperature on the microscale spatial variable; however, beginning in Section 3 when we derive macroscale equations for the homogenized problem, these variables will also depend on the global spatial variable x that denotes the location of the reference cell within the tree stem. Within a reference cell, the dynamics for $s_{iw}(t)$, $s_{gi}(t)$, $r(t)$ and $U(t)$ are governed by four differential equations whose derivation can be found in Ceseri & Stockie (2013). The first is the Stefan condition for the ice/water interface in the fiber

$$\partial_t s_{iw} = -\frac{D(E_2)}{E_w - E_i}\nabla_y T_2 \cdot \mathbf{n} + \frac{\partial_t U}{2\pi s_{iw} L^f}, \tag{2.1a}$$

where $T_2(y,t)$ denotes the microscale temperature variable that depends on both time and the local spatial variable $y \in Y^2$ (which needs to be distinguished from the macroscale temperature variable $T_1(x,t)$ introduced later) and $\nabla_y T_2 \cdot \mathbf{n}$ is the normal derivative at the interface. Here, the enthalpies of water and

ice (E_w and E_i, resp.) are evaluated at the freezing point, $T = T_c$; consequently, the difference $E_w - E_i$ represents the latent heat of fusion. We describe heat transport using a mixed temperature–enthalpy formulation, in which the thermal diffusion coefficient $D(E_2)$ is written as a function of enthalpy $E_2(y,t)$. Following Visintin (1996), we take D to have the piecewise affine linear form

$$D(E) = \begin{cases} \frac{k_i}{\rho_i}, & \text{if } E < E_i, \\ \frac{k_i}{\rho_i} + \frac{E-E_i}{E_w-E_i}\left(\frac{k_w}{\rho_w} - \frac{k_i}{\rho_i}\right), & \text{if } E_i \leqslant E < E_w, \\ \frac{k_w}{\rho_w}, & \text{if } E_w < E, \end{cases} \tag{2.1b}$$

where ρ_w, ρ_i are the densities of water and ice respectively, and k_w, k_i are the thermal conductivities. Note that D in this temperature–enthalpy formulation has units of $\mathrm{W\,m^2/kg\,K}$ and is referred to as a thermal diffusion coefficient, to distinguish it from the more usual "thermal diffusivity" (which is defined as the ratio $k/\rho c$ and has units of $\mathrm{m^2/s}$). The governing equations for T_2 and E_2 are discussed later in Sections 4.7–4.8 as a result of the two-scale convergence analysis and are the solutions of the system (4.20a–e). Note that the final term in the Stefan condition (2.1a) was neglected in Ceseri & Stockie (2013) and serves to capture the effect on the phase interface of fiber–water volume changes due to porous flow through the fiber/vessel wall.

The next two differential equations embody conservation of mass in the fiber

$$\partial_t s_{gi} = -\frac{(\rho_w - \rho_i)s_{iw}\partial_t s_{iw}}{s_{gi}\rho_i} + \frac{\rho_w \partial_t U}{2\pi s_{gi}\rho_i L^f}, \tag{2.1c}$$

and the vessel

$$\partial_t r = -\frac{N^f \partial_t U}{2\pi r L^v}. \tag{2.1d}$$

Note that within the sapwood there are many more fibers than vessels (as depicted in Figure 1a), so that the effect of fiber–vessel flux terms should be increased to account for the multiplicity of fibers. With this in mind, we have multiplied appropriate fluxes by the parameter N^f in (2.1d) that represents the average number of fibers per vessel and has a typical value of $N^f = 16$. The final differential equation describes water transport through the porous fiber/vessel wall in response to both hydraulic and osmotic pressure

$$\partial_t U = -\frac{\mathscr{L}A}{N^f}(p_w^v - p_w^f - \mathscr{R}C_s T_1). \tag{2.1e}$$

Here, we denote the pressure variable by p, where superscripts f/v refer to fiber/vessel and subscript w denotes the liquid water phase. The constant parameter $\mathscr{L}$ is the fiber/vessel wall conductivity, A is the wall surface area, C_s is the vessel sugar concentration, and $\mathscr{R}$ is the universal gas constant. Note that because U is defined inside Y^2, we should strictly be using the microscale temperature T_2 in the osmotic term in (2.1e), but this would lead to a significant complication in any numerical algorithm due an additional nonlinear coupling between scales. Therefore, we have used T_1 instead, which is a reasonable approximation because temperature variations throughout the reference cell are small.

Several intermediate variables have been introduced into the above equations. They are determined

by the following algebraic relations:

$$p_w^f = p_g^f(0) \left(\frac{s_{gi}(0)}{s_{gi}} \right)^2 - \frac{2\sigma}{s_{gi}}, \qquad \text{(Young–Laplace equation for fiber)} \qquad (2.2a)$$

$$p_w^v = p_g^v - \frac{2\sigma}{r}, \qquad \text{(Young–Laplace equation for vessel)} \qquad (2.2b)$$

$$p_g^v = \frac{\rho_g^v \mathscr{R} T_1}{M_g}, \qquad \text{(ideal gas law for vessel)} \qquad (2.2c)$$

$$\rho_g^v = \rho_g^v(0) \left(\frac{r(0)}{r} \right)^2. \qquad \text{(vessel gas density)} \qquad (2.2d)$$

All constant parameters appearing in the above equations are listed in Table 1 along with typical values.

There is one special case to consider, namely when a fiber initially containing an ice layer is above the freezing point for long enough time that the ice melts completely. In the moment the ice layer disappears, the reference cell geometry appears as in Figure 3b and the cell-level equations must be modified as follows. First of all, $D(E_2)$ must change to account for the fact that there are two possible values of thermal diffusivity, one in the region containing the gas and another in the liquid. Furthermore, the gas/ice and ice/water interfaces merge so that Eq. (2.1a) drops out and we identify a new fiber gas/water interface as $s_{gw} := s_{iw} \equiv s_{gi}$. This leads to the following simplified version of (2.1c)

$$\partial_t s_{gw} = \frac{\partial_t U}{2\pi s_{gw} L^f},$$

but otherwise the microscale equations (2.1)–(2.2) remain the same.

The equations for the temperature and enthalpy variables appearing in the microscale model above are derived in the next section in the context of a simpler problem involving only melting ice. Despite the fact that this reduced model involves only a single microscale variable for the dynamics of the ice–water interface s_{iw} (in addition to the temperature), the equations for temperature and enthalpy remain the same, and we will show that the microscale model above is completed by Eqs. (4.20a)–(4.20e).

3. Reduced model: Melting ice bars

We now shift our attention to the macroscale problem, which captures the dynamics of thawing sap within a cylindrical tree stem having a circular cross-section Ω. There is a clear separation of scales in that the tree has radius on the order of tens of centimetres whereas the cell-level processes occur over distances on the order of microns. Let $x \in \Omega$ represent the macroscale spatial variable and $y \in Y$ the microscale variable on the reference cell. Then, our main aim in this section is to determine equations for the temperature and enthalpy variables not only in the reference cell, $T_2(y,t)$ and $E_2(y,t)$, but also on the macroscale, $T_1(x,t)$ and $E_1(x,t)$.

The derivation of these equations may be simplified significantly by considering a reduced problem that involves only ice/water phase change and leaves out all other physical processes (porous flow, gas bubbles, surface tension, etc.). To this end, we consider a periodic array of melting "ice bars" as pictured in Figure 4a, situated inside a slightly more general domain $\Omega \subset \mathbb{R}^d$ having Lipschitz boundary that contains both water and ice in the form of circular inclusions. Let $Y = [0, \delta]^d$ be a *reference cell* that captures the configuration of the periodic microstructure, and for which δ represents its actual physical

Table 1. Constant parameter values appearing in the sap exudation model (taken from Ceseri & Stockie (2013)).

Symbol	Description	Value	Units
Geometric parameters:			
δ	Side length of reference cell	4.33×10^{-5}	m
γ	$= R^{\mathrm{f}} + W$, Radius of Γ	7.88×10^{-6}	m
R^{f}	Fiber radius	3.5×10^{-6}	m
R^{v}	Vessel radius	2.0×10^{-5}	m
L^{f}	Fiber length	1.0×10^{-3}	m
L^{v}	Vessel length	5.0×10^{-4}	m
V^{f}	Fiber volume $= \pi (R^{\mathrm{f}})^2 L^{\mathrm{f}}$	3.85×10^{-14}	m^3
V^{v}	Vessel volume $= \pi (R^{\mathrm{v}})^2 L^{\mathrm{v}}$	6.28×10^{-13}	m^3
A	Area of fiber/vessel wall $= 2\pi R^{\mathrm{f}} L^{\mathrm{f}}$	2.20×10^{-8}	m^2
W	Thickness of fiber/vessel wall	4.38×10^{-6}	m
N^{f}	Number of fibers per vessel	16	–
R_{tree}	Tree stem radius	0.25	m
Thermal parameters:			
c_{w}	Specific heat of water	4180	J/kg K
c_{i}	Specific heat of ice	2100	J/kg K
E_{w}	Enthalpy of water at T_{c}	9.07×10^5	J/kg
E_{i}	Enthalpy of ice at T_{c}	5.74×10^5	J/kg
k_{w}	Thermal conductivity of water	0.556	W/m K
k_{i}	Thermal conductivity of ice	2.22	W/m K
ρ_{w}	Density of water	1000	kg/m^3
ρ_{i}	Density of ice	917	kg/m^3
T_{c}	Freezing temperature for water	273.15	K
T_{a}	Ambient temperature $= T_{\mathrm{c}} + 10$	283.15	K
α	Heat transfer coefficient	10	W/m^{2}K
Other parameters:			
M_{g}	Molar mass of air	0.029	kg/mol
$\mathscr{R}$	Universal gas constant	8.314	J/mol K
σ	Gas/liquid surface tension	0.076	kg/s^2
C_{s}	Vessel sugar concentration (2%)	58.4	mol/m^3
$\mathscr{L}$	Hydraulic conductivity of fiber/vessel wall	5.54×10^{-13}	m^2 s/kg

size with $0 \leqslant \delta \ll 1$ (although we focus on dimension $d = 2$, the theoretical results proven here apply to any dimension). The reference cell is divided into two sub-domains Y^1 and Y^2 that are separated by a Lipschitz boundary $\Gamma = Y^1 \cap Y^2$ as shown in Figure 4b. For simplicity, we take Γ to be a circle of radius γ satisfying $0 < \gamma < \frac{1}{2}\delta$. The primary feature that we exploit in our homogenization approach is that within Y^1 heat must diffuse rapidly, whereas in Y^2 there is a relatively slow diffusion of heat.

(a) Periodically-tiled domain Ω (b) Reference cell Y for reduced model
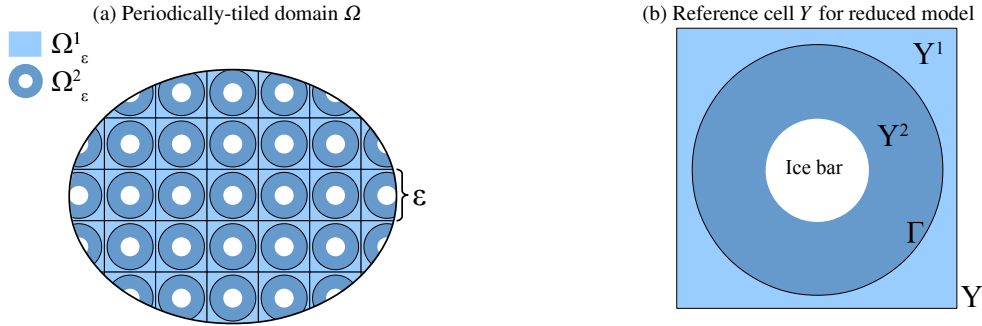
Figure 4. Periodic microstructure of the reduced model for melting ice bars immersed in water. (a) The tree stem cross-section Ω is tiled periodically with copies of the reference cell Y, each of which is scaled to have side length ε. The homogenization process then takes the limit as $\varepsilon \to 0$. (b) The reference cell Y for the reduced model, illustrating the decomposition into fast (Y^1 and Ω_ε^1) and slow (Y^2 and Ω_ε^2) diffusing regions, with $Y = Y^1 \cup Y^2 \cup \Gamma$.

We next introduce a small parameter $0 < \varepsilon \ll 1$ that corresponds to the size of the periodic microstructure (and must be distinguished from the physical size δ because we will eventually take the limit as $\varepsilon \to 0$). The domain Ω may then be decomposed into three ε-dependent sub-domains: $\Omega_\varepsilon^1 := \mathrm{int}\bigcup_{k\in\mathbb{Z}^d} \varepsilon(k + \overline{Y^1}) \cap \Omega$ (which is connected), and two disconnected components consisting of the region $\Omega_\varepsilon^2 := \bigcup_{k\in\mathbb{Z}^d} \varepsilon(k + Y^2) \cap \Omega$ and the boundary curves $\Gamma_\varepsilon := \bigcup_{k\in\mathbb{Z}^d} \varepsilon(k + \Gamma) \cap \Omega$. This decomposition is illustrated in Figure 4. To avoid technical difficulties, we assume that Γ_ε does not touch the outer boundary of Ω, so that $\Gamma_\varepsilon \cap \partial\Omega = \emptyset$ and $\Omega_\varepsilon^2 \cap \partial\Omega = \emptyset$.

The major advantage of this reduced model is that the reference cell problem simplifies significantly, with the only unknowns being s_{iw} and temperature. We proceed with the temperature and enthalpy equations.

3.1 Temperature and enthalpy equations

Throughout the analytical developments of this paper, we employ what is known as the two-phase formulation of the Stefan problem, in which the heat diffusion equation is posed in a mixed form involving both temperature and enthalpy. Assuming that material properties of water and ice remain constant, the temperature T can be written as a piecewise linear function of enthalpy E as follows (Visintin, 1996)

$$
T = \widetilde{\omega}(E) = \begin{cases} \dfrac{1}{c_{\mathrm{i}}}E, & \text{if } E < E_{\mathrm{i}}, \\[2mm] T_{\mathrm{c}}, & \text{if } E_{\mathrm{i}} \leqslant E < E_{\mathrm{w}}, \\[2mm] T_{\mathrm{c}} + \dfrac{1}{c_{\mathrm{w}}}(E - E_{\mathrm{w}}), & \text{if } E_{\mathrm{w}} \leqslant E, \end{cases}
$$

where c_w and c_i denote specific heats of water and ice respectively, and $T_c = 273.15K$ is the freezing point of water (parameter values are listed in Table 2). A distinguishing feature of this temperature–enthalpy relationship is that when temperature is equal to the freezing point, the enthalpy varies while temperature remains constant – this behavior derives from the fact that a certain amount of energy (called latent heat) is required to effect a change in phase from solid to liquid at the phase interface.

Because the function $\widetilde{\omega}(E)$ is neither differentiable nor invertible, we instead employ in our model a regularized version $\omega(E)$ defined as

$$T = \omega(E) = \begin{cases} \dfrac{1}{c_i}E, & \text{if } E < E_{i-}, \\[2mm] \text{[smooth connection]}, & \text{if } E_{i-} \leqslant E < E_{i+}, \\[2mm] T_c - \dfrac{2E - (E_{i+} + E_{w-})}{2c_\infty}, & \text{if } E_{i+} \leqslant E < E_{w-}, \\[2mm] \text{[smooth connection]}, & \text{if } E_{w-} \leqslant E < E_{w+}, \\[2mm] T_c + \dfrac{1}{c_w}(E - E_{w+}), & \text{if } E_{w+} \leqslant E, \end{cases} \tag{3.1}$$

which has "rounded corners" that are smoothed over the short intervals $E_{i-} \lesssim E_i \lesssim E_{i+}$ and $E_{w-} \lesssim E_w \lesssim E_{w+}$. Note that we have also introduced a small positive slope $c_\infty^{-1} \ll 1$ within the central plateau region near $T \approx T_c$ (refer to Figure 5). These modifications ensure that ω is a continuously differentiable, invertible and monotone increasing function of enthalpy. Incidentally, such a regularized function is most likely a more accurate representation of what one would actually observe in a real physical system.
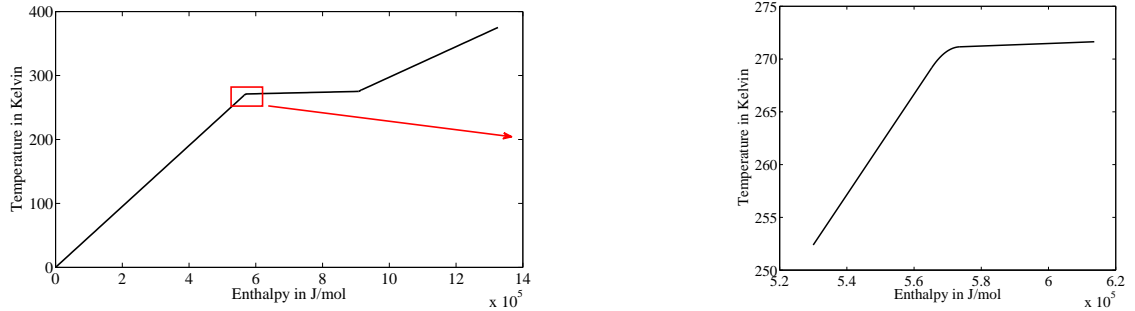

Figure 5. Regularized temperature–enthalpy function, $T = \omega(E)$, for a generic ice/water phase change problem in which the critical (freezing) temperature is $T_c = 273.15K$. The zoomed-in view on the right illustrates the smoothed corners in the regularization.

We now describe the solution decomposition into slow and fast diffusing variables. Let functions $T_{1,\varepsilon}$ and $E_{1,\varepsilon}$ denote the fast-diffusing temperature and enthalpy components respectively, with both defined on the sub-region Ω_ε^1. Similarly, let $T_{2,\varepsilon}$ and $E_{2,\varepsilon}$ denote the slowly-diffusing temperature and enthalpy on Ω_ε^2. We may then state the strong formulation of the two-phase Stefan problem as

$$\partial_t E_{1,\varepsilon} - \nabla \cdot [D(E_{1,\varepsilon})\nabla T_{1,\varepsilon}] = 0 \qquad \text{in } \Omega_\varepsilon^1, \tag{3.2a}$$

$$D(E_{1,\varepsilon})\nabla T_{1,\varepsilon} \cdot \mathbf{n} = -\varepsilon^2 D(E_{2,\varepsilon})\nabla T_{2,\varepsilon} \cdot \mathbf{n} \qquad \text{on } \Gamma_\varepsilon, \tag{3.2b}$$

$$-D(E_{1,\varepsilon})\nabla T_{1,\varepsilon} \cdot \mathbf{n} = \alpha(T_{1,\varepsilon} - T_a) \qquad \text{on } \partial\Omega \cap \partial\Omega_\varepsilon^1, \tag{3.2c}$$

$$\partial_t E_{2,\varepsilon} - \varepsilon^2 \nabla \cdot [D(E_{2,\varepsilon})\nabla T_{2,\varepsilon}] = 0 \qquad \text{in } \Omega_\varepsilon^2, \tag{3.2d}$$

$$E_{2,\varepsilon} = E_{1,\varepsilon} \qquad \text{on } \Gamma_\varepsilon, \tag{3.2e}$$

where $D(E)$ is given by (2.1b) and T_a is the ambient temperature imposed on the outer domain boundary. Note that these equations capture the phase interface location implicitly through the relationship $T = \omega(E)$ and no explicit Stefan-type phase interface condition is imposed.

4. Two-scale homogenization of the reduced model

It is not feasible to solve the system of equations (3.2) derived in the previous section using direct numerical simulations owing to the presence of the microstruture with ε being very small. This section contains the primary theoretical results pertaining to an upscaling of the reduced problem which is achieved by characterising the limit as $\varepsilon \to 0$. Lemmas and theorems are stated here, and the proofs are relegated to the Appendix.

4.1 *Weak formulation*

In order to make the problem ameanable to periodic-homogenization techniques, we begin by transforming Eqs. (3.2) into a weak formulation. To avoid technical difficulties, we replace the Robin boundary condition (3.2c) by a Dirichlet condition $E_{1,\varepsilon} = \omega^{-1}(T_a)$ (i.e., we consider the formal limit $\alpha \to \infty$) and refer the reader to Graf & Peter (2014) for a detailed discussion. This requires first defining some appropriate solution spaces:

$$\mathscr{V}_\varepsilon^1 := \left\{ u \in L^2([0,t_m], \mathscr{H}^1(\Omega_\varepsilon^1)) \cap \mathscr{H}^1([0,t_m], \mathscr{H}^1(\Omega_\varepsilon^1)') \mid u = 0 \text{ on } \partial\Omega_\varepsilon^1 \cap \partial\Omega \right\},$$

$$\mathscr{V}_\varepsilon^2 := \left\{ u \in L^2([0,t_m], \mathscr{H}^1(\Omega_\varepsilon^2)) \cap \mathscr{H}^1([0,t_m], \mathscr{H}^1(\Omega_\varepsilon^2)') \mid u = 0 \text{ on } \Gamma_\varepsilon \right\},$$

$$\mathscr{V} := L^2([0,t_m], \mathscr{H}_0^1(\Omega)) \cap \mathscr{H}^1([0,t_m], \mathscr{H}^1(\Omega)'),$$

where the "primes" denote dual spaces and $[0,t_m]$ represents the time interval of interest for some fixed $t_m > 0$. The corresponding test spaces are $V_\varepsilon^1 = \{u \in \mathscr{H}^1(\Omega_\varepsilon^1) \mid u = 0 \text{ on } \partial\Omega_\varepsilon^1 \cap \partial\Omega\}$, $V_\varepsilon^2 = \mathscr{H}_0^1(\Omega_\varepsilon^2)$ and $V = \mathscr{H}_0^1(\Omega)$. We also need to introduce notation for inner products, with $(u,v)_{\Omega_\varepsilon^\alpha} = \int_{\Omega_\varepsilon^\alpha} uv \, dx$ representing the L^2-inner product with respect to space of two functions in $\mathscr{V}_\varepsilon^\alpha$ for $\alpha = 1,2$, whereas $(u,v)_{\Omega_\varepsilon^\alpha, t} = \int_0^t \int_{\Omega_\varepsilon^\alpha} uv \, dx \, d\tau$ denotes that an additional time integration is performed over the interval $[0,t]$ with $0 \leqslant t \leqslant t_m$. Finally, we let $\langle u,v \rangle_{\Gamma_\varepsilon} = \langle u,v \rangle_{H^{\frac{1}{2}}(\Gamma_\varepsilon)' \times H^{\frac{1}{2}}(\Gamma_\varepsilon)}$ denote the dual pairing on Γ_ε. Later, we will show that $D(E_{2,\varepsilon})\nabla T_{2,\varepsilon} \cdot \mathbf{n} \in L^2(\Gamma_\varepsilon)$, so that we can interpret $\langle u,v \rangle_{\Gamma_\varepsilon}$ as $\int_{\Gamma_\varepsilon} g_\varepsilon uv \, dS$, where g_ε represents the Riemann curvature tensor.

We are now prepared to state the weak form of the heat-diffusion problem. Assuming that initial values $T_{1,\varepsilon,\text{init}} = \omega(E_{1,\varepsilon,\text{init}})$ and $T_{2,\varepsilon,\text{init}} = \omega(E_{2,\varepsilon,\text{init}})$ are smooth, non-negative and bounded functions, and that a Dirichlet condition $T_{1,\varepsilon} = T_a$ is imposed at the outer boundary $\partial\Omega \cap \partial\Omega_\varepsilon^1$, our goal is to find $(T_{1,\varepsilon}, T_{2,\varepsilon}) \in (\mathscr{V}_\varepsilon^1 + T_a) \times (\mathscr{V}_\varepsilon^2 + T_{1,\varepsilon})$ such that

$$(\partial_t E_{1,\varepsilon}, \varphi)_{\Omega_\varepsilon^1} + (D(E_{1,\varepsilon})\nabla T_{1,\varepsilon}, \nabla\varphi)_{\Omega_\varepsilon^1} + \varepsilon^2 \langle D(E_{2,\varepsilon})\nabla T_{2,\varepsilon} \cdot \mathbf{n}, \varphi \rangle_{\Gamma_\varepsilon} = 0, \tag{4.1a}$$

$$(\partial_t E_{2,\varepsilon}, \psi)_{\Omega_\varepsilon^2} + (\varepsilon^2 D(E_{2,\varepsilon})\nabla T_{2,\varepsilon}, \nabla\psi)_{\Omega_\varepsilon^2} = 0, \tag{4.1b}$$

for all $\varphi, \psi \in V_\varepsilon^1 \times V_\varepsilon^2$. Note that $\mathbf{n}$ represents the outward-pointing unit normal vector on Γ_ε, and that temperature and enthalpy are connected via $T_{\alpha,\varepsilon} = \omega(E_{\alpha,\varepsilon})$, or equivalently $E_{\alpha,\varepsilon} = \omega^{-1}(T_{\alpha,\varepsilon})$. We

assume that $\omega^{-1}(T_a)$ is positive, bounded and smooth such it can be extended to $[0,t_m] \times \Omega$ in $\mathscr{H}^1$. We note again in closing that slow diffusion is induced in the problem via the factor ε^2 multiplying terms in Eqs. (4.1) that involve the diffusion coefficient $D(E_{2,\varepsilon})$.

4.2   *Transformation of the model*

In this section, we apply a procedure developed by Arbogast et al. (1990) to transform the model (4.1) by combining enthalpies $E_{1,\varepsilon}$ and $E_{2,\varepsilon}$ into a single function Θ_ε defined on the whole ε-independent domain Ω. We use the fact that Γ_ε is the only boundary of Ω_ε^2 to obtain

$$\langle \varepsilon^2 D(E_{2,\varepsilon})\nabla T_{2,\varepsilon} \cdot \mathbf{n}, \psi \rangle_{\Gamma_\varepsilon} = (\varepsilon^2 \nabla \cdot [D(E_{2,\varepsilon})\nabla T_{2,\varepsilon}], \psi)_{\Omega_\varepsilon^2} + (\varepsilon^2 D(E_{2,\varepsilon})\nabla T_{2,\varepsilon}, \nabla \psi)_{\Omega_\varepsilon^2}$$
$$= (\partial_t E_{2,\varepsilon}, \psi)_{\Omega_\varepsilon^2} + (\varepsilon^2 D(E_{2,\varepsilon})\nabla T_{2,\varepsilon}, \nabla \psi)_{\Omega_\varepsilon^2},$$
(4.2)

for all $\psi \in V$. After substituting this expression into (4.1a) we obtain

$$(\partial_t E_{1,\varepsilon}, \varphi)_{\Omega_\varepsilon^1} + (D(E_{1,\varepsilon})\nabla T_{1,\varepsilon}, \nabla \varphi)_{\Omega_\varepsilon^1} + (\partial_t E_{2,\varepsilon}, \psi)_{\Omega_\varepsilon^2} + (\varepsilon^2 D(E_{2,\varepsilon})\nabla T_{2,\varepsilon}, \nabla \psi)_{\Omega_\varepsilon^2} = 0,$$

for all $\varphi, \psi \in V_\varepsilon^1 \times V_\varepsilon^2$. Hence, Eqs. (4.1) have been replaced with

$$(\partial_t E_{1,\varepsilon} + \partial_t E_{2,\varepsilon}, \varphi)_\Omega + (D(E_{1,\varepsilon})\nabla T_{1,\varepsilon} + \varepsilon^2 D(E_{2,\varepsilon})\nabla T_{2,\varepsilon}, \nabla \varphi)_\Omega = 0,$$
$$E_{1,\varepsilon} = E_{2,\varepsilon} \quad \text{on } \Gamma_\varepsilon,$$
(4.3)

for all $\varphi \in V$. We then define the function $\Theta_\varepsilon \in L^2([0,t_m], \mathscr{H}^1(\Omega))$ by

$$\Theta_\varepsilon = \left\{ \begin{array}{ll} E_{1,\varepsilon} & \text{in } \Omega_\varepsilon^1, \\ E_{2,\varepsilon} & \text{in } \Omega_\varepsilon^2, \end{array} \right.$$

so that with conditions (3.2b) and (3.2e) the function Θ_ε is guaranteed to be continuous and weakly differentiable. Furthermore, we define $\kappa_\varepsilon = \chi_{1,\varepsilon} + \varepsilon^2 \chi_{2,\varepsilon}$ where $\chi_{i,\varepsilon}$ for $i = 1,2$ are indicator functions for Ω_ε^1 and Ω_ε^2 respectively. Solving (4.1) is then equivalent to finding $\Theta_\varepsilon \in (\mathscr{V} + \omega^{-1}(T_a))$ such that

$$(\partial_t \Theta_\varepsilon, \varphi)_\Omega + (\kappa_\varepsilon D(\Theta_\varepsilon)\omega'(\Theta_\varepsilon)\nabla \Theta_\varepsilon, \nabla \varphi)_\Omega = 0,$$
(4.4)

for all $\varphi \in V$, where we have used that $T_{1,\varepsilon} = \omega(E_{1,\varepsilon})$ and $T_{2,\varepsilon} = \omega(E_{2,\varepsilon})$.

We perform one further transformation of (4.4) that makes the Dirichlet boundary condition homogeneous. To this end, we define $\rho_\varepsilon = \Theta_\varepsilon - \omega^{-1}(T_a)$ where $\omega^{-1}(T_a)$ is extended continuously to Ω. Then (4.4) is equivalent to finding $\rho_\varepsilon \in \mathscr{V}$ such that

$$(\partial_t \rho_\varepsilon, \varphi)_\Omega + (\kappa_\varepsilon D \omega'(\rho_\varepsilon + \omega^{-1}(T_a))\nabla \rho_\varepsilon, \nabla \varphi)_\Omega = (-\partial_t \omega^{-1}(T_a), \varphi)_\Omega,$$
(4.5)

for all $\varphi \in V$.

4.3   *Existence of a weak solution*

4.3.1   *Theorem of existence*   To prove the existence of a solution to (4.4) for every $\varepsilon > 0$, we formulate a theorem of existence, which is strongly inspired by a proof for a related result found in a set of unpublished lecture notes by Wolff (2016). In Theorem 4.1 we introduce a general existence result for

parabolic equations with non-monotone non-linearities in the diffusion operator. The proof is based on the Rothe method. We state the theorem next and provide the proof in Appendix A.1.

Consider the initial–boundary value problem

$$\partial_t u + \sum_{j=1}^{n} \partial_{x_j} \left(a(x,t,u)\partial_{x_j}u \right) = F(x,t) \qquad \text{in } S \times \Omega, \tag{4.6a}$$

$$u = 0 \qquad \text{on } S \times \partial\Omega, \tag{4.6b}$$

$$u(0,x) = u_0(x) \qquad \text{in } \Omega, \tag{4.6c}$$

with

$$\Omega \subset \mathbb{R}^n \quad \text{bounded Lipschitz domain}, \qquad S = [0, t_{\mathrm{m}}], \tag{4.7a}$$

$$a(x,t,u): \Omega \times S \times \mathbb{R} \to \mathbb{R} \quad \text{Bochner-measurable in } x \text{ and continuous in } t \text{ and } u, \tag{4.7b}$$

$$\exists\, 0 < \lambda \leqslant \Lambda < \infty \text{ such that } \lambda \leqslant a(x,t,u) \leqslant \Lambda \;\; \forall s \in \mathbb{R}, \text{ for a.e. } t \in \mathbb{R} \text{ and a.e. } x \in \Omega, \tag{4.7c}$$

$$V = \mathscr{H}_0^1(\Omega), \qquad \mathscr{V} = L^2(S,V), \qquad \mathscr{V}^* = L^2(S,V^*), \tag{4.7d}$$

$$u_0 = L^2(\Omega), \qquad F \in \mathscr{V}^*. \tag{4.7e}$$

LEMMA 4.1 Let the conditions (4.7) be satisfied. Then

$$\langle A(t)(u,v), w \rangle = \sum_{j=1}^{n} \int_{\Omega} a(x,t,u)\, \partial_{x_j}v\, \partial_{x_j}w\, \mathrm{d}x, \tag{4.8}$$

$$\langle f, v \rangle = \int_0^T \int_{\Omega} F(x,t)\, v(x,t)\, \mathrm{d}x\, \mathrm{d}t, \tag{4.9}$$

define a family of operators $A(t): V \times V \to V^*$ and an element $f \in \mathscr{V}^*$ for which the following hold:

$$\forall\, u,v \in V, \text{ for a.e. } t \in \mathbb{R}: \quad \|A(t)(u,v)\|_{V^*} \leqslant \Lambda\, \|v\|_V, \tag{4.10a}$$

$$\forall\, u \in V, \text{ for a.e. } t \in \mathbb{R}: \quad A(t)(u,\cdot): V \to V^* \text{ is linear and continuous}, \tag{4.10b}$$

$$\forall\, u,v \in V, \text{ for a.e. } t \in \mathbb{R}: \quad \langle A(t)(u,v), v \rangle \geqslant \lambda\, \|v\|_V^2, \tag{4.10c}$$

$$\mathscr{A}: \mathscr{V} \times \mathscr{V} \to \mathscr{V}^* \qquad \text{is the realization of } A \text{ with } \mathscr{A}(u,u) = A(t)(u,u). \tag{4.10d}$$

This lemma can be proven using standard arguments as described by Dautray & Lions (2000) and Wolff (2016). Lemma 4.1 implies that any initial value problem of the form

$$\begin{aligned} u' + \mathscr{A}(u,u) &= f \qquad \text{in } V^*, \\ u(0) &= u_0, \end{aligned} \tag{4.11}$$

which includes the problem (4.6), is well-defined.

THEOREM 4.1 Consider equation (4.6) satisfying the conditions (4.7). Then there exists at least one solution of equation (4.11).

The proof of Theorem 4.1 is given in Appendix A.1. We apply this theorem to the reduced model (4.5) for which the space V is $\mathscr{H}_0^1(\Omega)$, so that both solution and test space correspond to $\mathscr{V} = L^2([0,t_{\mathrm{m}}], \mathscr{H}_0^1(\Omega))$. We have $u_0 = \rho_\varepsilon(0)$ and $f \equiv \partial_t \omega^{-1}(T_{\mathrm{a}})$, which is in $\mathscr{V}^*$ by assumption. The function a corresponding to the problem (4.5) is

$$a(x,t,u) = \kappa_\varepsilon(x) D\omega'(u + \omega^{-1}(T_{\mathrm{a}}(t))),$$

which satisfies the conditions (4.7) for $u \in V$. With all conditions of Theorem 4.1 fulfilled, we obtain the following result

COROLLARY 4.1 There exists a solution of Eq. (4.5).

4.4 *A priori estimates and limit functions*

Our main results on a priori estimates are stated in Lemma 4.2 below, which bounds independently of ε the functions $E_{1,\varepsilon}$ and $T_{1,\varepsilon}$ in $L^2([0,t_{\mathrm{m}}], \mathscr{H}^1(\Omega_\varepsilon^1))$, and similarly $E_{2,\varepsilon}$ and $T_{2,\varepsilon}$ in $L^2([0,t_{\mathrm{m}}], \mathscr{H}^1(\Omega_\varepsilon^2))$. The proof of this Lemma is given in Appendix A.2.

LEMMA 4.2 There exists a constant C_1, independent of ε, such that the solution Θ_ε of (4.4) (equivalently, $E_{1,\varepsilon}$ and $E_{2,\varepsilon}$ of (4.3)) satisfies

$$\|\Theta_\varepsilon\|_\Omega^2 + \|\kappa_\varepsilon \nabla \Theta_\varepsilon\|_{\Omega,t}^2 = \|E_{1,\varepsilon}\|_{\Omega_\varepsilon^1}^2 + \|\nabla E_{1,\varepsilon}\|_{\Omega_\varepsilon^1,t}^2 + \|E_{2,\varepsilon}\|_{\Omega_\varepsilon^2}^2 + \varepsilon^2 \|\nabla E_{2,\varepsilon}\|_{\Omega_\varepsilon^2,t}^2 \leqslant C_1.$$

Using standard results of two-scale convergence (Allaire, 1992; Nguetseng, 1989; Peter & Böhm, 2008), we immediately obtain the following result.

LEMMA 4.3 There exist functions $E_{1,0} \in L^2([0,t_{\mathrm{m}}], \mathscr{H}^1(\Omega))$, $\widehat{E}_{1,0} \in L^2([0,t_{\mathrm{m}}], L^2(\Omega, \mathscr{H}_\#^1(Y^1)))$ and $E_{2,0} \in L^2([0,t_{\mathrm{m}}], L^2(\Omega, \mathscr{H}_\#^1(Y^2)))$ such that, up to subsequences,

$$E_{1,\varepsilon} \xrightarrow{\text{2-scale}} E_{1,0},$$

$$\nabla E_{1,\varepsilon} \xrightarrow{\text{2-scale}} \nabla_x E_{1,0} + \nabla_y \widehat{E}_{1,0},$$

$$E_{2,\varepsilon} \xrightarrow{\text{2-scale}} E_{2,0},$$

$$\nabla E_{2,\varepsilon} \xrightarrow{\text{2-scale}} \nabla_y E_{2,0}.$$

Note that $E_{1,0}$ is independent of y, and we have also introduced $\widehat{E}_{1,0} \in L^2([0,t_{\mathrm{m}}], L^2(\Omega, \mathscr{H}_\#^1(Y^1)))$ and $E_{2,0} \in L^2([0,t_{\mathrm{m}}], L^2(\Omega, \mathscr{H}_\#^1(Y^2)))$, where the subscript # denotes Y-periodicity in space. The limit of $\nabla E_{1,\varepsilon}$ has a special form obtained in Allaire (1992) that consists of two terms: one involving a gradient with respect to the slow variable, and a second term with respect to the fast variable.

4.5 *Identification of the two-scale limit*

Owing to the nonlinear dependence of the diffusion coefficient on enthalpy in (4.5), we have not yet been able to identify the system of equations satisfied by the limit functions of Lemma 4.3 without further assumptions. In order to allow the limit passage without difficulties, we *assume* in the remainder of this section that the function $D\omega'$ in (4.5) is independent of Θ_ε, which makes the model linear. Note that having strong convergence of the function Θ_ε in $L^2([0,t_{\mathrm{m}}], \Omega)$ would lead to the same results. A homogenization proof for the fully nonlinear problem is left for future work.

In order to characterize the limit functions from Lemma 4.3, we define test functions that vary on length scales of size $O(1)$ and $O(\varepsilon)$ according to

$$\varphi_\varepsilon \left(x, \tfrac{x}{\varepsilon} \right) = \chi_1 \left(\tfrac{x}{\varepsilon} \right) \left(\varphi_0(x) + \varepsilon \varphi_1 \left(x, \tfrac{x}{\varepsilon} \right) \right) + \chi_2 \left(\tfrac{x}{\varepsilon} \right) \varphi_2(x, \tfrac{x}{\varepsilon}),$$

where $(\varphi_0, \varphi_1, \varphi_2) \in C_0^\infty(\Omega) \times C^\infty(\Omega, C_\#^\infty(Y)) \times C^\infty(\Omega, C_\#^\infty(Y))$.

By substituting φ_ε into (4.1a) and using χ_i to write the resulting integrals over the entire domain Ω, we obtain

$$\int_\Omega \chi_1\left(\tfrac{x}{\varepsilon}\right)\partial_t E_{1,\varepsilon}(x,t)\varphi_\varepsilon\left(x,\tfrac{x}{\varepsilon}\right)dx + \int_\Omega \chi_1\left(\tfrac{x}{\varepsilon}\right)D\omega'\nabla E_{1,\varepsilon}(x,t)\nabla\varphi_\varepsilon\left(x,\tfrac{x}{\varepsilon}\right)dx$$
$$+ \int_\Omega \chi_2\left(\tfrac{x}{\varepsilon}\right)\partial_t E_{2,\varepsilon}(x,t)\varphi_\varepsilon\left(x,\tfrac{x}{\varepsilon}\right)dx + \int_\Omega \chi_2\left(\tfrac{x}{\varepsilon}\right)D\omega'\varepsilon^2\nabla E_{2,\varepsilon}(x,t)\varphi_\varepsilon\left(x,\tfrac{x}{\varepsilon}\right)dx = 0.$$

Then, taking the limit as $\varepsilon \to 0$ yields

$$\int_{\Omega\times Y^1}\partial_t E_{1,0}(x,t)\varphi_0(x)\,dy\,dx + \int_{\Omega\times Y^1}D\omega'[\nabla_x E_{1,0}(x,t)+\nabla_y\widehat{E}_{1,0}(x,y,t)][\nabla_x\varphi_0(x)+\nabla_y\varphi_1(x,y)]\,dy\,dx$$
$$+ \int_{\Omega\times Y^2}\partial_t E_{2,0}(x,y,t)\varphi_2(x,y)\,dy\,dx + \int_{\Omega\times Y^2}D\omega'\nabla_y E_{2,0}(x,y,t)\nabla_y\varphi_2(x,y)\,dy\,dx = 0, \quad (4.12)$$

where y denotes the spatial variable on the reference cell Y.

We are free at this point to choose any test function and so we take $\varphi_0 = 0$ and $\varphi_2 = 0$ in Eq. (4.12). To start with, we introduce functions $\mu_k \in \mathscr{H}^1_\#(Y^1)$ in order to express $\widehat{E}_{1,0}(x,y,t) = \sum_{k=1}^d \partial_{x_k}E_{1,0}(x,t)\mu_k(y)$ in separable form. The weak formulation of the cell problem for $k = 1,\ldots,d$ may then be expressed in the simpler form

$$(e_k + \nabla_y\mu_k,\ \nabla_y\varphi_1)_{Y^1} = 0, \tag{4.13}$$

where the μ_k are Y-periodic. Alternatively, we may take $\varphi_1 = 0$ in Eq. (4.12) to obtain

$$\int_{\Omega\times Y^1}\partial_t E_{1,0}(x,t)\varphi_0(x)\,dy\,dx + \int_{\Omega\times Y^1}D\omega'\sum_{k=1}^d\partial_{x_k}E_{1,0}(x,t)[e_k+\nabla_y\mu_k(y)]\nabla_x\varphi_0(x)\,dy\,dx$$
$$+ \int_{\Omega\times Y^2}\partial_t E_{2,0}(x,y,t)\varphi_2(x,y)\,dy\,dx + \int_{\Omega\times Y^2}D\omega'\nabla_y E_{2,0}(x,y,t)\nabla_y\varphi_2(x,y)\,dy\,dx = 0,$$

which can be rewritten in the more suggestive form

$$\int_{\Omega\times Y^1}\partial_t E_{1,0}(x,t)\varphi_0(x)\,dy\,dx + \int_\Omega D\omega'\sum_{k,\ell=1}^d\partial_{x_k}E_{1,0}(x,t)\int_{Y^1}[\delta_{k\ell}+\partial_{y_\ell}\mu_k(y)]\,dy\,\partial_{x_\ell}\varphi_0(x)\,dx$$
$$+ \int_{\Omega\times Y^2}\partial_t E_{2,0}(x,y,t)\varphi_2(x,y)\,dy\,dx + \int_{\Omega\times Y^2}D\omega'\nabla_y E_{2,0}(x,y,t)\nabla_y\varphi_2(x,y)\,dy\,dx = 0. \quad (4.14)$$

The diffusion term involves the factors

$$\Pi_{k\ell} = \int_{Y^1}(\delta_{k\ell}+\partial_{y_\ell}\mu_k)\,dy \tag{4.15}$$

for $k,\ell = 1,\ldots,d$, which can be represented as a matrix Π that multiplies the diffusion coefficient $D\omega'$. We then obtain from (4.12) and (4.14) the equation

$$|Y^1|(\partial_t E_{1,0},\ \varphi_0)_\Omega + (\Pi D\omega'\nabla_x E_{1,0},\ \nabla_x\varphi_0)_\Omega + (\partial_t E_{2,0},\ \varphi_2)_{\Omega\times Y^2} + (D\omega'\nabla_y E_{2,0},\ \nabla_y\varphi_2)_{\Omega\times Y^2} = 0.$$
$$\tag{4.16}$$

As a final step, we obtain the limit equation for $E_{2,0}$ by setting $\varphi_0 = 0$ in Eq. (4.16), and similarly for $E_{1,0}$ by setting $\varphi_2 = 0$ in Eq. (4.16), which is found using a similar transition as in (4.2). The resulting limit equations are

$$|Y^1|(\partial_t E_{1,0},\ \varphi_0)_\Omega + (\Pi D\omega'\nabla_x E_{1,0},\ \nabla_x\varphi_0)_\Omega + \langle D\omega'\nabla_y E_{2,0},\ \varphi_0\rangle_{\Gamma\times\Omega} = 0, \qquad (4.17\text{a})$$

$$(\partial_t E_{2,0},\ \varphi_2)_{\Omega\times Y^2} + (D\omega'\nabla_y E_{2,0},\ \nabla_y\varphi_2)_{\Omega\times Y^2} = 0, \qquad (4.17\text{b})$$

for all $\varphi_0 \in \mathscr{H}_0^1(\Omega)$ and $\varphi_2 \in L^2(\Omega,\mathscr{H}_\#^1(Y^2))$, where Π is the $d\times d$ matrix of scaling factors defined in (4.15), $E_{1,0} \in L^2([0,t_m],\mathscr{H}^1(\Omega))$ with $\omega(E_{1,0}) = T_a$ on $\partial\Omega$, and $E_{2,0} \in L^2([0,t_m],L^2(\Omega,\mathscr{H}_\#^1(Y^2)))$ with $E_{2,0} = E_{1,0}$ on $\Omega\times\Gamma$.

To simplify notation in the remainder of the paper, we drop the zero subscripts in $\{T_{1,0},E_{1,0},T_{2,0},E_{2,0}\}$ and denote them instead by $\{T_1,E_1,T_2,E_2\}$. Note again that we have only rigorously derived the limit problem in the linear case and so we would need to prove strong convergence of the function Θ_ε in $L^2([0,t_m],\Omega)$ for the analysis to hold for (4.4); we will nevertheless transition back to the nonlinear problem with an enthalpy-dependent diffusion coefficient $D\omega'(E)$, for which the corresponding limit equations are

$$|Y^1|(\partial_t E_1,\ \varphi_0)_\Omega + (\Pi D(E_1)\omega'(E_1)\nabla_x E_1,\ \nabla_x\varphi_0)_\Omega + \langle D(E_2)\omega'(E_2)\nabla_y E_2,\ \varphi_0\rangle_{\Gamma\times\Omega} = 0, \qquad (4.18\text{a})$$

$$(\partial_t E_2,\ \varphi_2)_{\Omega\times Y^2} + \big(D(E_2)\omega'(E_2)\nabla_y E_2,\ \nabla_y\varphi_2\big)_{\Omega\times Y^2} = 0. \qquad (4.18\text{b})$$

4.6 *Uniqueness*

The uniqueness of the solution to the nonlinear problem (4.18) subject to suitable boundary and initial conditions may be formulated compactly in terms of the following theorem, which is proven in Appendix A.3.

THEOREM 4.2 Equations (4.18) have at most one solution given by

$$T_1 \in \mathscr{V}^1(\Omega) + T_a \qquad = \left(L^2\left([0,t_m],\mathscr{H}_0^1(\Omega)\right) + T_a\right) \cap \mathscr{H}^1\left([0,t_m],L^2(\Omega)\right),$$

$$T_2 \in \mathscr{V}^2(\Omega\times Y^2) + T_1 = \left(L^2\left([0,t_m],L^2(\Omega,\mathscr{H}_0^1(Y^2))\right) + T_1\right) \cap \mathscr{H}^1\left([0,t_m],L^2(\Omega\times Y^2)\right),$$

where $T_1 = \omega(E_1)$ and $T_2 = \omega(E_2)$.

We note that the uniqueness of the limit problem implies that already the whole sequences of solutions converge to the functions satisfying (4.18).

4.7 *Strong formulation of the limit problem*

We now state an equivalent strong formulation of the limit problem corresponding to the weak form in (4.18), but with the Dirichlet condition at the outer boundary switched back to a Robin condition again. This consists of a PDE for T_1 and E_1 on the macroscale domain Ω

$$|Y^1|\partial_t E_1 - \nabla_x\cdot(\Pi D(E_1)\nabla_x T_1) = \int_\Gamma D(E_2)\nabla_y T_2\cdot\mathbf{n}\,dS \qquad \text{in } \Omega, \qquad (4.19\text{a})$$

$$-D(E_1)\nabla_x T_1\cdot\mathbf{n} = \alpha(T_1 - T_a) \qquad \text{on } \partial\Omega, \qquad (4.19\text{b})$$

along with a second PDE for T_2 and E_2 on the microscale

$$\partial_t E_2 - \nabla_y\cdot(D(E_2)\nabla_y T_2) = 0 \text{ on } \Omega\times Y^2, \qquad (4.19\text{c})$$

$$T_2 = T_1 \ \text{ on } \Omega\times\Gamma, \qquad (4.19\text{d})$$

and initial values for enthalpy that we denote $E_{1,\text{init}}$ and $E_{2,\text{init}}$. These two problems are coupled through the heat flux integral term in (4.19a) and the matching condition (4.19d), both of which are enforced on Γ. This is again the *two-phase formulation of the Stefan problem*, which contains no explicit equation for the motion of the phase interface; instead, the interface location is captured implicitly through the temperature–enthalpy relation

$$T_1 = \omega(E_1) \text{ in } \Omega \qquad \text{and} \qquad T_2 = \omega(E_2) \text{ in } \Omega \times Y^2. \tag{4.19e}$$

Under the assumption that temperature within the ice phase is constant in space during a thawing event (Visintin, 1996), the problem (4.19) may be rewritten in an equivalent *one-phase formulation* that obeys the same macroscale problem

$$|Y^1|\partial_t E_1 - \nabla_x \cdot (\Pi D(E_1)\nabla_x T_1) = \int_\Gamma D(E_2)\nabla_y T_2 \cdot \mathbf{n}\, dS \quad \text{in } \Omega, \tag{4.20a}$$

$$-D(E_1)\nabla_x T_1 \cdot \mathbf{n} = \alpha(T_1 - T_a) \qquad \text{on } \partial\Omega. \tag{4.20b}$$

On the reference cell, however, the ice temperature is taken equal to T_c and the water temperature obeys the following microscale equations

$$c_w \partial_t T_2 - \nabla_y \cdot (D(E_2)\nabla_y T_2) = 0 \qquad \text{on } \Omega \times \widetilde{Y}^2(x,t), \tag{4.20c}$$

$$T_2 = T_1 \qquad \text{on } \Omega \times \Gamma, \tag{4.20d}$$

$$T_2 = T_c \quad \text{on } \Omega \times \partial\widetilde{Y}^2(x,t), \tag{4.20e}$$

which are solved only on the water-filled annular region $\widetilde{Y}^2(x,t) \subseteq Y^2$ lying between Γ and the moving phase boundary $s_{\text{iw}}(x,t)$. Consequently, in this one-phase formulation both the domain $\widetilde{Y}^2$ and its boundary $\partial\widetilde{Y}^2$ depend on x and t through s_{iw}. In the case of a freezing event, the ordering of the ice/water layers is reversed in which case the water temperature is held constant at T_c instead and $\widetilde{Y}^2$ corresponds to the sub-region containing ice. Finally, rather than imposing a temperature–enthalpy relation, the one-phase formulation fixes the temperature on the phase boundary via (4.20e) and provides an explicit Stefan condition governing the dynamics of the phase interface

$$\partial_t s_{\text{iw}} = -\frac{D(E_2)}{(E_w - E_i)}\nabla_y T_2 \cdot \mathbf{n} \quad \text{on } \Omega \times \partial\widetilde{Y}^2(x,t). \tag{4.20f}$$

The primary reason that we employ the one-phase formulation of the Stefan problem is that it makes numerical simulations of the limit problem much more convenient. A detailed derivation of this one-phase formulation from the corresponding two-phase formulation can be found in Visintin (1996).

4.8 *Limit problem for the sap exudation model*

Based on the limit problem we just derived for the reduced model using homogenization techniques, it is now straightforward to pose the analogous limit problem for the sap exudation model. The two-scale heat transport equations (4.20a)–(4.20e) remain identical, but the Stefan condition (4.20f) in the reduced model is replaced by the full set of differential–algebraic equations (DAEs) (2.1)–(2.2) for the microscale sap exudation problem.

Although we have only performed the periodic homogenization procedure on the reduced model, there are several features of the sap exudation problem that can be exploited to extend our analytical results:

1. *Presence of the gas phase:* which takes the form of gas bubbles in both fiber and vessel and introduces a spatial dependence in the thermal diffusion coefficient, $D(E,x)$. Extending our analytical results to the case when D also depends on x would be a straightforward generalization.

2. *Dissolved sugar in the vessel sap:* which gives rise to an osmotic potential between fiber and vessel that is essential for generating realistic exudation pressures. Sugar within the vessel sap also depresses the freezing point so that the function ω in (3.1) differs between vessel and fiber. Although we do not need to consider freezing point depression explicitly in this paper (since we treat only a single thawing cycle) this effect could still be incorporated into the analysis, for example by adding an extra spatial dependence in ω. Alternatively, the fiber could be defined as separate domain that is connected to the vessel via appropriate boundary conditions, thereby ensuring that the homogenization results carry through for the sap exudation model. We have chosen not to incorporate this effect into the analysis, although periodic homogenization has previously been applied to Stefan problems having various functional forms for ω in Bossavit & Damlamian (1981).

3. *Extension to a freezing cycle:* which requires modifications only to the microscale equations in the reference cell as outlined in Graf et al. (2015). Consequently, this extension has no effect on the homogenization procedure.

5. Multiscale numerical simulations

5.1 *Solution algorithm*

We now propose a multiscale numerical solution algorithm that computes approximate solutions to both the reduced and sap exudation models. The method is based on a time-splitting approach that alternates in each time step between solving the microscale (reference cell) and macroscale equations, and exploits three main approximations:

- Because of the simple form of coupling between microscale and macroscale problems that involves only interfacial solution values, we propose a "frozen coefficient" splitting approach in which variables on the microscale are advanced to the next time step by holding all macroscale variables constant at their previous values, and vice versa.

- The multiplier matrix Π defined in (4.13) for the thermal diffusion coefficient in the macroscale heat equation is independent of the local temperature state and phase interface configuration. Consequently, the entries $\Pi_{k\ell}$ are constants that only need to be computed once at the beginning of a simulation.

- Both models have an inherent radial symmetry on the microscopic scale, and we restrict ourselves here to problems that have an analogous symmetry on the macroscale. This is a natural choice for the tree sap exudation problem since a tree stem is well-approximated by a circular cylinder with cross-section Ω having radius R_{tree}. Consequently, all variables and governing equations are cast in terms of a single radial coordinate labelled x or y on the macro- or microscale respectively, so that only 1D problems need to be solved on both scales.

The spatial discretization of the governing equations is performed separately on each spatial scale:

Macroscale heat problem: The circular domain Ω is discretized on an equally-spaced radial mesh of $M = 40$ points, denoted $x_i = iR_{\text{tree}}/M$ for $i = 0, 1, \ldots, M - 1$. Discrete values of the unknowns $T_1(x,t)$ and $E_1(x,t)$ are defined at each mesh point x_i.

Microscale heat problem: Within each reference cell Y, the portion of the domain $Y^2(x,t)$ consisting of ice will grow or shrink according to the location of the local phase boundary s_{iw}. We therefore employ a *moving mesh* discretization wherein the annular-shaped water region in the fiber is discretized at m equally-spaced radial points that move in time according to $y_j(t) = s_{\text{iw}}(t) + j(\gamma - s_{\text{iw}}(t))/m$ for $j = 0, 1, \ldots, m$, where we recall that γ is the radius of the artificial boundary Γ. In practice, it suffices to use a coarse grid in the reference cell with $m = 4 \ll M$. Discrete values of the solution variables $T_2(x,y,t)$ and $E_2(x,y,t)$ are then defined at each location x_i and y_j.

Recall that the temperature T_2 is treated as the primary solution variable in the microscale problem, whereas enthalpy E_1 is the primary variable in the macroscale problem. We employ a method-of-lines approach in which spatial derivatives of solution quantities in both x and y are approximated using finite differences. The resulting coupled system of time-dependent DAEs is then integrated in time using the stiff ODE solver `ode15s` (MATLAB, 2015). This solver requires absolute and relative error tolerances, which we choose as `AbsTol = 7e-8` and `RelTol = 2e-14`.

We may then summarize the multiscale numerical algorithm as follows:

Step 1: For a single canonical reference cell having the shape of a square with a circular hole, we use the package COMSOL Multiphysics (COMSOL, 2015) to discretize the domain, approximate the functions $\mu_i(y)$ in (4.13), and then to calculate the corresponding integrals in (4.15). This yields precomputed constant values of the four entries in matrix Π that are used in the remainder of the computation (in Step 3c).

Step 2: At each macroscale point x_i, set the initial value of $T_2 = T_{2,\text{init}}$. Then within the ith reference cell, set $E_1 = E_{1,\text{init}}$ at each point y_j, and initialize either s_{iw} for the reduced model or $\{s_{\text{iw}}, s_{\text{gi}}, r, U\}$ for the sap exudation model. Initial values are listed in Table 2.

Step 3: At each time step, advance the solution variables as follows:

   3a. Set $T_1 = \omega(E_1)$ and $E_2 = \omega^{-1}(T_2)$.

   3b. Update T_2 by integrating the microscale heat diffusion problem (4.20c)–(4.20e) one time step within each reference cell $Y^2(x_i,t)$. The values of T_1, E_1, E_2 and s_{iw} are frozen at the previous time step.

   3c. Update E_1 by integrating the macroscale heat diffusion problem (4.20a)–(4.20b) at all grid points x_i. Due to radial symmetry of the reference cell, the integral in the right hand side of (4.20a) reduces to $2\pi R_2 D(E_2)\nabla T_2 \cdot \mathbf{n}$ where R_2 is the radius of Y^2. The values of T_2 and E_2 are frozen at the values computed in step 3b.

   3d. Update the microscale variables within each reference cell $\widetilde{Y}^2(x_i,t)$ by integrating the governing differential(–algebraic) equations in time, and freezing values of T_1 and T_2. Here, the equations being solved depend on the model problem:

   - For the reduced problem, include the reduced Stefan condition (4.20f) only.
   - For the sap exudation problem, use the system of DAEs (2.1)–(2.2).

Table 2. Initial values for the reduced and sap exudation models, taken from Ceseri & Stockie (2013).

Symbol	Description	Initial Values	Units
T_{init}	Initial temperature	T_c	K
T_a	Ambient temperature	$T_c + 10$	K
$s_{\text{iw}}(0)$	$= R^f$	3.5×10^{-6}	m
$s_{\text{gi}}(0)$	$= R^f/\sqrt{2}$	2.5×10^{-6}	m
$r(0)$		6.0×10^{-6}	m
$U(0)$		0	m^3
$p_g^f(0)$		2.0×10^5	N/m^2
$p_g^v(0)$		1.0×10^5	N/m^2
$p_w^f(0)$		9.89×10^4	N/m^2
$p_w^v(0)$		9.95×10^4	N/m^2

3e. Increment the time variable and return to Step 3a.

The above algorithm must be modified slightly whenever the ice completely melts, since the loss of the Stefan condition (4.20f) induces a change in the governing equations. At the same time, the separation of the reference cell into two sub-domains Y^1 and Y^2 (which was required to handle the Dirichlet condition on temperature at the phase interface) is no longer necessary and hence the temperature can be described by the single field T_1 that obeys (4.20a)–(4.20b) with zero right hand side, constant D, and $\Pi \equiv 1$. This alteration to the governing equations can be triggered easily within the numerical algorithm above by exploiting the "event detection" feature in Matlab's `ode15s` solver, signalling an event based on a zero-crossing of the ice layer thickness, $b = s_{\text{iw}} - s_{\text{gw}}$: when $b > 0$, ice is still present and the original equations are solved; when $b = 0$, ice is totally melted and the modified equations just described are solved instead (and Steps 3b and 3d are omitted). We mention in closing that although only 2D simulations are performed in this paper, our algorithm extends in a straightforward manner to 3D stem geometries by stacking a number of 2D stem slices in series and enforcing suitable flux continuity conditions.

5.2 *Simulations of the reduced model*

We begin by presenting numerical simulations of the reduced model wherein a periodic array of melting ice bars fills a circular domain Ω with radius $R_{\text{tree}} = 0.25$ m. The periodic reference cell $Y = [0, \delta]^2$ depicted in Figure 4b is given a side length of $\delta = 4.33 \times 10^{-5}$ m. Each reference cell is initialized with an ice bar of radius $s_{\text{iw}}(0) = R^f/\sqrt{2}$ surrounded by water, such that the initial volume of ice in the reduced model and the sap exudation model is equal. The initial temperature throughout the domain is set to $T_1(x,0) = T_2(x,y,0) = T_{\text{init}} = T_c$. On the outer boundary of the domain, a Robin boundary condition $-D(E_1(R_{\text{tree}},t))\nabla_x T_1(R_{\text{tree}},t) \cdot \mathbf{n} = \alpha(T_1(R_{\text{tree}},t) - T_a)$ is imposed with $T_a = T_c + 10$, while a symmetry condition $\partial_x T_1(0,t) = 0$ is imposed at the center of the domain. We take the size of the artificial boundary Γ in each reference cell to be larger than the fiber radius R^f by an amount equal to the typical thickness $W = 4.38 \times 10^{-6}$ m of the vessel wall; in other words, $\gamma = R^f + W$ which is well-separated from the phase interface. Note that the system is solved in dimensional variables so that there is no need to non-dimensionalize and hence the size of the reference cell corresponds simply to the physical dimension δ. All physical parameter values and initial conditions are listed in Tables 1 and 2.

Figure 6 displays a sequence of solution snapshots at selected times between 0 and 16 h that illustrate

the spatial and temporal variations in the macroscale temperature T_1 and ice-bar radius s_{iw}. In each plot, the horizontal (x) axis corresponds to the radial distance measured from the center of the circular domain Ω. As time progresses, the temperature gradually increases and penetrates the domain interior as heat from the outer boundary diffuses inwards. In response to this rise in temperature, the ice melts and the ice bar within each local reference cell shrinks in size. The ice bars in the outermost region melt first, and by time $t \approx 16$ h the entire domain is completely melted (i.e., $s_{iw} = 0$ throughout Ω). The formation of a steep thawing front that progresses from the outer boundary to the center of the domain is clearly visible in Figure 6b. These results should be contrasted with the study in Ceseri & Stockie (2013) that investigated only the local behaviour of the solution to the thawing model (at some fixed location on the microscale); on the other hand, our homogenized model results illustrate the progress of the thawing front on the macroscale, while at the same time incorporating physical processes taking place on the microscale.
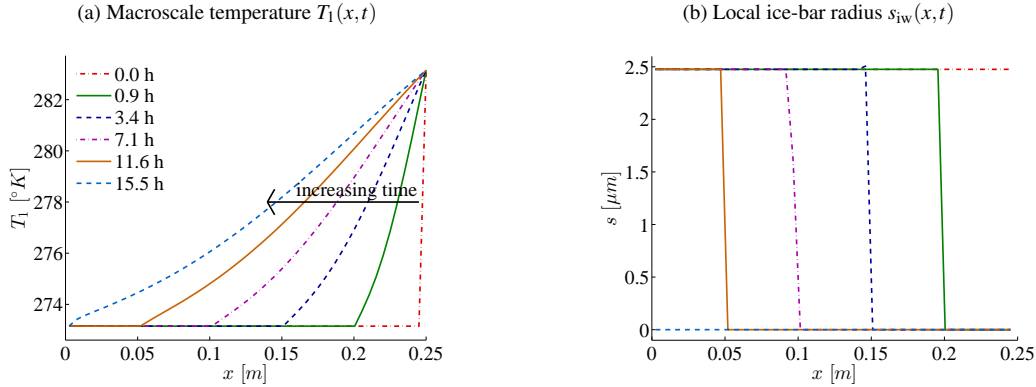
(a) Macroscale temperature $T_1(x,t)$ (b) Local ice-bar radius $s_{iw}(x,t)$

Figure 6. Simulations of the reduced model, showing T_1 and s_{iw} as functions of the global variable x, pictured at selected times between 0 and 16 h.

5.3 *Simulations of the sap exudation model*

Next we perform simulations of the sap exudation model for a tree stem with the same parameters and boundary conditions as for the reduced model. Recall that we chose the length of the reference cell to be $\delta = 4.33 \times 10^{-5}$ m, consistent with the size of fibers and vessels in actual sapwood. The initial temperature is again taken to be $T_{init} = T_c$ throughout, with the water in the fiber initially frozen and the vessel sap in liquid form. Recall that this initial state captures the effect of freezing point depression due to the presence of sugar within the vessel sap; and besides setting these initial conditions, there is no need to incorporate any concentration dependence in the freezing point for this thawing-only model. To initiate a thawing cycle, we apply the Robin boundary condition at the outer boundary of the tree stem as in the reduced model, $-D(E_1(R_{tree},t))\nabla_x T_1(R_{tree},t) \cdot \mathbf{n} = \alpha(T_1(R_{tree},t) - T_a)$, where $T_a = T_c + 10$. All other parameters and initial values specific to the sap exudation model can be found in Tables 1 and 2.

After applying the multiscale algorithm described in Section 5.1, the solutions for T_1, s_{iw} and s_{gi}, r, U, p_w^f and p_w^v are illustrated in Figure 7 at a sequence of six times between 0 and 1.4 h. From these plots, it is evident that the solution dynamics for all variables are characterized by a *melting front* that progresses through the tree from the outer boundary toward the center (from right to left in the plots) as the warm ambient air gradually heats up the interior. Furthermore, the time required for complete
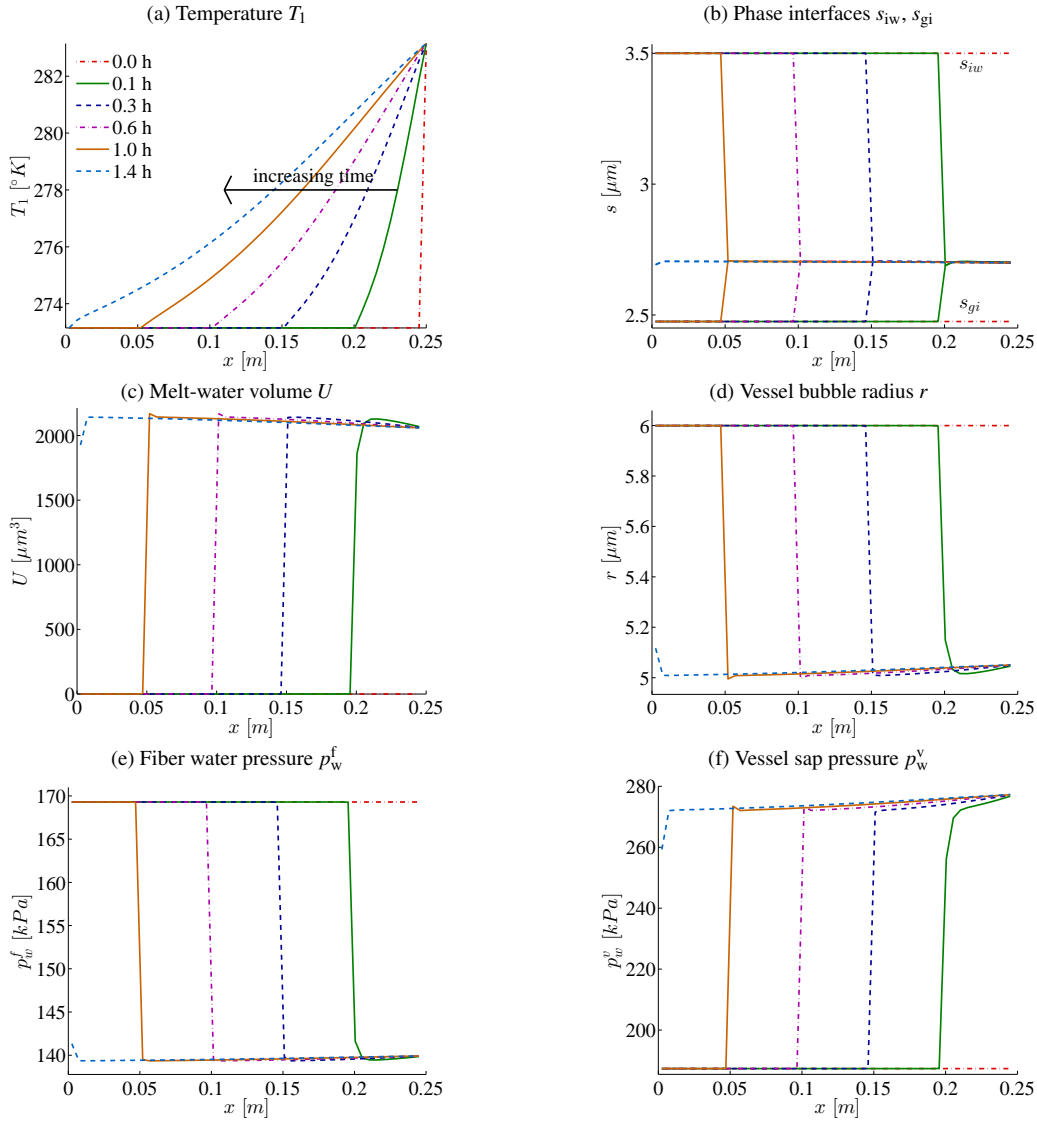
Figure 7. Simulations of the sap exudation model showing (x,t)-dependent solution profiles at a sequence of time points. In all cases, the profiles evolve from right to left (toward the center of the tree) as indicated by the arrow in (a).

melting of the ice contained in the fibers is just under 1.4 h.

The temperature profiles vary smoothly in space as one expects from a diffusion problem, while the other solution quantities are characterized by a steep front that propagates toward the centre of the tree with a speed that decreases with time. The steepness of the melting front derives from the thawing of ice and subsequent adjustment of liquid between vessels and fibers on the microscale, all of which occur very rapidly in the instant after the temperature exceeds the freezing point T_c at any given location x. The reason for the gradual slowing of the melting front with time is that the heat flux naturally decreases as the front approaches the center of the tree, which in turn leads to a speed decrease owing to the Stefan condition.

We also observe a clear separation in time scales between the slow evolution of temperature on the macroscale and the relatively rapid phase change and sap redistribution within fibers and vessels on the microscale. This scale separation is easily seen by comparing Figure 7 with plots of the time evolution of local solution variables at a fixed radial location $x = 0.15$ m shown in Figure 8. The thickness of the fiber–ice layer can be determined as the vertical distance between the s_{iw} and s_{gi} curves in Figure 8b, which rapidly drops to zero as the ice melts. At the same time, melt-water is driven from fiber to vessel by the pressure stored in the fiber gas bubble, and the pressure plot in Figure 8c clearly illustrates the subsequent increase in p_w^v that we attribute to exudation pressure. After the melting process is complete, the vessel–liquid pressure continues to increase (although at a slow rate that is not easily visible to the naked eye) owing to a slight expansion of gas in the fiber and vessel in response to further temperature increase as heat continues to diffuse through the liquid phase from the outer tree surface.
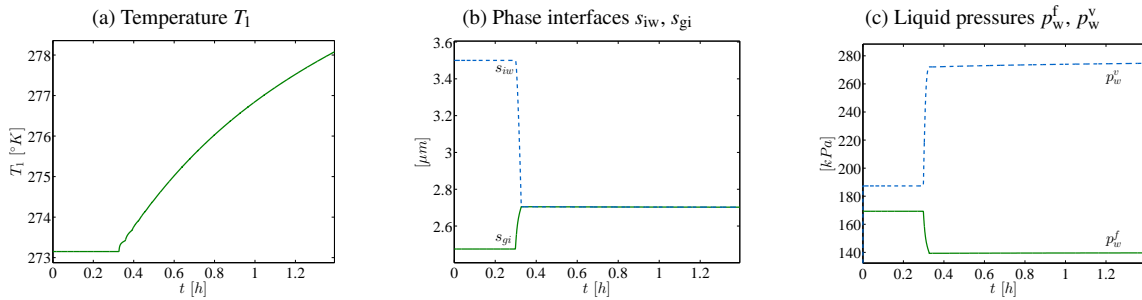

Figure 8. Simulations of the sap exudation model, showing the time evolution of various solution components at the fixed radial position $x = 0.15$ m.

Upon more careful inspection of the gas/ice and ice/water interfaces in Figure 8b, we observe that there is a slight time delay in the motion of s_{iw} relative to s_{gi}. Indeed, the ice begins to melt at the gas/ice interface (leading to an increase in s_{gi}) at a time that is roughly 25 s in advance of when s_{wi} starts to drop, which is when a water layer appears between the ice and fiber wall. This phenomenon can be explained as follows. When melt-water first appears in a particular fiber, the gas bubble pressure is so high that water is immediately forced out into the vessel, leaving the ice layer in contact with the fiber wall. The gas pressure then declines until approximately 25 s elapses, at which time the rate of water melting exceeds that of the porous outflow and a water layer begins to accumulate along the fiber wall. By this time, roughly half of the water volume contained in the fiber has been transferred into the vessel.

One of the most significant results from our sap exudation model is the prediction that vessel liquid pressure increases by roughly 120 kPa, which is within the range of exudation pressures actually observed in sugar maple trees (Cirelli et al., 2008) and closely-related species such as black walnut

(Améglio et al., 2001). Furthermore, simulations of multiple freeze and thaw cycles with this homogenized model yield results that are consistent with controlled experiments on walnut (Graf et al., 2015). Work is currently underway on comparing our model results to experiment measurements of sugar maple saplings (Brown, 2015).

Finally, we draw a comparison between the solution of the sap exudation model for temperature T_1 and ice layer thickness $s_{iw} - s_{gi}$, and the corresponding solution variables (T_1, s_{iw}) from the reduced problem in Section 3. Although the shape of the temperature and ice interface profiles are similar, there is a significant difference in that the melting process for the reduced problem takes over 10 times longer than for the sap exudation problem even though the macroscopic domain and outer temperature are the same. This discrepancy may seem at first glance to be inconsistent, but this result can be easily explained as follows. The diffusion coefficient for the sap exudation problem is roughly 10 times higher because of the much larger value of thermal diffusivity ($k/\rho c$) in the gas phase (with an upper bound of 2×10^{-5} m^2/s based on atmospheric conditions) compared with the corresponding values for ice and water (1.2×10^{-6} and 1.3×10^{-7} m^2/s respectively) which are the only phases appearing in the reduced model.

6. Conclusions

The aim of this paper was to apply techniques from periodic homogenization to derive a multiscale model for a multiphase flow problem arising in the context of maple sap exudation. Because of the complexity of the physics underlying the sap exudation problem (involving liquid/ice phase change, dissolving gas, flow through porous cell membranes, osmosis and other effects), we started by deriving a simpler reduced model that focuses on the melting of a periodic array of ice bars. This reduced model belongs to the class of Stefan problems, which have been well-studied in the context of homogenization in case of fast diffusion. We prove results on existence, uniqueness and a priori estimates for the weak form of the reduced governing equations involving fast *and* slow diffusion, which we then use to derive a strong form of the homogenized limit problem in which there is a clear separation between equations for the cellular level processes on the microscale, and heat transport on the macroscale. Our approach has the advantage that it applies homogenization techniques in a straightforward manner in order to obtain an uncomplicated limit model. The primary novelty of the analytical results, relative to other work on homogenization of Stefan-type problems, derives from our directly imposing a Dirichlet condition on temperature at the phase interface, which gives rise to a decomposition into fast and slow variables on the sub-regions Y^1 and Y^2 of the reference cell. A major advantage of this decomposition is that it leads immediately to a simple and efficient numerical method based on a time-splitting approach that exploits the scale separation in the limit equations. In particular, we are able to encapsulate all microscale processes specific to the phase change within the reference cell domain Y^2, wherein the temperature diffuses slowly. Consequently, this homogenized limit structure (and the corresponding numerical algorithm) can be easily adapted to the sap exudation problem by simply "plugging in" the corresponding microscale equations governing the cell-level processes. In passing, we proved a general existence result for quasi-linear parabolic differential equations having a non-monotone nonlinearity in the diffusion operator. Numerical simulations are performed for both the sap exudation problem and the reduced model, and the results are shown to be consistent, although there are significant differences that we attribute to the absence of a gas phase in the reduced model. The homogenized limit equations derived here have been extended elsewhere (Graf et al., 2015) to handle the freezing case, and then applied to simulate multiple daily cycles of freeze and thaw cycles; these results show an excellent match with sap exudation experiments.

There are several natural avenues for future work that arise from this study. Most notably, we would like to fill the gap in our analytical results by extend the proofs to handle the nonlinearity arising from an enthalpy-dependent thermal diffusion coefficient. This effort will be guided by results on other related nonlinear problems (Kanschat-Krebs, 2015; Visintin, 2007). We also plan to extend our model to handle the three-dimensional geometry of a cylindrical tree stem and include radial flow of sap and the effect of gravitational pressure head on vertical transport.

A. Proofs of three main results

This appendix contains proofs of the lemmas and theorems introduced in Section 4. Throughout, we use C or C_i to denote a generic, real, positive constant whose value may change from line to line.

A.1   *Proof of existence*

THEOREM 4.1 Consider equation (4.6) satisfying the conditions (4.7). Then there exists at least one solution of equation (4.11).

Proof.

(i) To handle the nonlinearities of A we perform the semi-discretization

$$\frac{u^m - u^{m-1}}{k} + A(mk)(u^{m-1}, u^m) = f^m \qquad \text{in } V^*, \tag{A.1}$$

for $m = 1, \ldots, N$, with $N \in \mathbb{N}$, $N > 2$, $k = \frac{t_m}{N}$, $u^0 = u_0$ and

$$f^m = \frac{1}{k} \int_{J_m} f(t) \, dt,$$

for $m = 1, \ldots, N$ and $J_m = [(m-1)k, mk]$. Then $f_k(t) = f^m$ on J_m for $m = 1, \ldots, N$. With these conditions the existence of the semi-discrete problem (A.1) holds.

(ii) (A priori estimates) We define the functions $u_k : [0, T] \to V$ and $w_k : [0, T] \to L^2(\Omega)$ with

$$u_k(t) = u^m, \tag{A.2a}$$

$$w_k(t) = u^m + \frac{t - mk}{k}(u^{m+1} - u^m). \tag{A.2b}$$

Then it holds that

$$\|u_k - w_k\|^2_{L^2(S, L^2(\Omega))} \leqslant \frac{k}{3} \sum_{m=1}^{N} \|u^m - u^{m-1}\|^2_{L^2(\Omega)}. \tag{A.3}$$

For the next estimate we start with the fact that

$$2(a - b, a) = \|a\|^2_\Omega - \|b\|^2_\Omega + \|a - b\|^2_\Omega \quad \forall \, a, b \in L^2(\Omega),$$

which implies

$$\|u^m\|^2_\Omega - \|u^{m-1}\|^2_\Omega + \|u^m - u^{m-1}\|^2_\Omega + 2k\langle A(mk)(u^{m-1}, u^m), u^m \rangle_{V^*V} = 2k\langle f^m, u^m \rangle_{V^*V}. \tag{A.4}$$

Using Hölder's inequality we obtain that

$$\|u^m\|_\Omega^2 - \|u^{m-1}\|_\Omega^2 + \|u^m - u^{m-1}\|_\Omega^2 + k\lambda\|u^m\|_V^2 \leqslant \frac{k}{\lambda}\|f^m\|_{V^*}^2. \tag{A.5}$$

Making use of the inequality

$$k\sum_{m=1}^{N}\|f^m\|_{V^*}^2 \leqslant \int_0^T \|f(t)\|_{V^*}^2\,\mathrm{d}t, \tag{A.6}$$

and then summing (A.5) over m from 1 to $r \leqslant N$ yields

$$\|u^r\|_\Omega^2 + \sum_{m=1}^{r}\|u^m - u^{m-1}\|_\Omega^2 + k\lambda\sum_{m=1}^{r}\|u^m\|_V^2 \leqslant \|u_0\|^2 + \frac{1}{\lambda}\int_0^T \|f(t)\|_{V^*}^2\,\mathrm{d}t. \tag{A.7}$$

It then follows that

$$\|u^r\|_\Omega^2 \leqslant \|u_0\|_\Omega^2 + \frac{1}{\lambda}\int_0^T \|f(t)\|_{V^*}^2\,\mathrm{d}t \quad \text{for } 1 \leqslant r \leqslant N, \tag{A.8a}$$

$$\sum_{m=1}^{r}\|u^m - u^{m-1}\|_\Omega^2 \leqslant \|u_0\|_\Omega^2 + \frac{1}{\lambda}\int_0^T \|f(t)\|_{V^*}^2\,\mathrm{d}t, \tag{A.8b}$$

$$k\sum_{m=1}^{r}\|u^m\|_V^2 \leqslant \frac{1}{\lambda}\|u_0\|_\Omega^2 + \frac{1}{\lambda^2}\int_0^T \|f(t)\|_{V^*}^2\,\mathrm{d}t. \tag{A.8c}$$

Using (A.8a) we obtain the estimates

$$\|u_k\|_{L^\infty(S,L^2(\Omega))} \leqslant c, \tag{A.9a}$$

$$\|w_k\|_{L^\infty(S,L^2(\Omega))} \leqslant c, \tag{A.9b}$$

where the constant c depends only on the right-hand side of (A.8a). Because of

$$\int_0^T \|u_k(t)\|_V^2\,\mathrm{d}t = k\sum_{m=1}^{N}\|u^m\|_V^2,$$

it follows that

$$\|u_k\|_{L^2(S,V)} \leqslant c. \tag{A.10}$$

The Banach space $L^\infty(S,L^2(\Omega))$ is the dual space of the separable space $L^1(S,L^2(\Omega))$; hence, when taken together with the estimates (A.9) and (A.10) and the theorems of Eberlein–Shmuljan and Banach–Alaoglu, we are guaranteed the existence of subsequences

$$u_k \rightharpoonup u \quad \text{in } L^2(S,V), \tag{A.11a}$$

$$u_k \rightharpoonup^* u \quad \text{in } L^\infty(S,L^2(\Omega)), \tag{A.11b}$$

$$w_k \rightharpoonup^* w \quad \text{in } L^\infty(S,L^2(\Omega)). \tag{A.11c}$$

We next want to show that

$$u = w. \tag{A.12}$$

Using (A.3) and (A.8a) we conclude that

$$u_k - w_k \to 0 \quad \text{in } L^2(S, L^2(\Omega)), \tag{A.13}$$

so that for a subsequence

$$u_k(t) - w_k(t) \to 0.$$

With Eqs. (A.9) we obtain that

$$u_k - w_k \to 0 \quad \text{in } L^\infty(S, L^2(\Omega)),$$

and hence we can rewrite (A.11c) as

$$w_k \rightharpoonup^* u \quad \text{in } L^\infty(S, L^2(\Omega)).$$

The nonlinearity of A requires another a priori estimate to perform the limit $k \to 0$. From (A.3), (4.7e) and (4.10a) we deduce that

$$\left\| \frac{u^m - u^{m-1}}{k} \right\|_{V^*} \leqslant \|f^m\|_{V^*} + \Lambda \|u^m\|_V. \tag{A.14}$$

After that, we apply (A.6) and (A.8c) to obtain

$$k \sum_{m=1}^{N} \left\| \frac{u^m - u^{m-1}}{k} \right\|_{V^*}^2 \leqslant d < \infty, \tag{A.15}$$

where d only depends on the data in (4.7e) and constants λ and Λ. This estimate implies that

$$\|w_k'\|_{L^2(S, V^*)} \leqslant d. \tag{A.16}$$

Eq. (A.11a) and the construction of w_k in (A.2a) yield

$$\forall \delta > 0 \quad \forall k \leqslant \delta : \quad \|w_k\|_{L^2(]\delta, T[, V)} \leqslant c, \tag{A.17}$$

for c independent of δ. When taken together with (A.16), (A.13), and the theorem of Lions–Aubin, we obtain subsequences

$$w_k \to u \quad \text{in } L^2(]\delta, T[, L^2(\Omega)), \tag{A.18a}$$

$$u_k - w_k \to 0 \quad \text{in } L^2(S, L^2(\Omega)), \tag{A.18b}$$

$$u_k \to u \quad \text{in } L^2(]\delta, T[, L^2(\Omega)). \tag{A.18c}$$

Then there exist a subsequence (u_k), converging pointwise a.e. on S to u. Using (A.11a) and Lebesgue's theorem we obtain

$$u_k \to u \quad \text{in } L^2(S, L^2(\Omega)). \tag{A.19}$$

(iii) (Limit) We define a translation of the function $u_k : [0, T] \to V$ by

$$u_k(t - k) := u^{m-1} \quad \text{on } J_m \quad \text{for } m = 1, \dots, N, \tag{A.20}$$

for $J_m = [(m-1)k, mk]$. Then the semi-discretization yields

$$w_k'(t) + A(t)(u_k(t-k), u_k(t)) = f_k(t) \quad \text{for a.e. } t \in S \quad \text{in } V^*. \tag{A.21}$$

Applying (A.21) to $v \in \mathcal{V}$ with $\mathcal{V}^* \subset L^2(S, L^2(\Omega))$ and $v(T) = 0$, and integrating over S using integration by parts in the first term yields

$$-\int_0^T (v'(t), w_k(t)) \, dt + \int_0^T \langle A(t)(u_k(t-k), u_k(t)), v(t) \rangle \, dt = \int_0^T \langle f_k(t), v(t) \rangle \, dt + (u_0, v(0)). \tag{A.22}$$

With (4.10a) and (A.11a) it holds for a subsequence that

$$A(\cdot)(u_k(\cdot - k), u_k(\cdot)) \rightharpoonup \zeta \quad \text{in } V^*. \tag{A.23}$$

Taking the limit in (A.22) we obtain

$$-\int_0^T (v'(t), u(t)) \, dt + \int_0^T \langle \zeta(t), v(t) \rangle \, dt = \int_0^T \langle f(t), v(t) \rangle \, dt + (u_0, v(0)). \tag{A.24}$$

With $u \in \mathcal{V}$, Eq. (A.24) and $u' \in \mathcal{V}^*$ yield

$$u'(t) + \zeta(t) = f(t) \quad \text{for a.e. } t \in S, \quad \text{in } V^*. \tag{A.25}$$

It is left to show that

$$A(t)(u, u) = \zeta. \tag{A.26}$$

We use the monotonicity of A in the second argument and compactness from the a priori estimates to obtain

$$X_k := \int_0^T \langle A(t)(u_k(t-k), u_k(t)) - A(t)(u_k(t-k), v(t)), u_k(t) - v(t) \rangle \, dt \geqslant 0 \tag{A.27}$$

for all $v \in \mathcal{V}$. Eq. (A.25) then implies

$$\int_0^T \langle f(t), u(t) \rangle \, dt + \frac{1}{2} \|u_0\|_\Omega^2 - \frac{1}{2} \|u(T)\|_\Omega^2 = \int_0^T \langle \zeta(t), u(t) \rangle \, dt, \tag{A.28}$$

and from Eq. (A.21) we obtain

$$\int_0^T \langle w_k'(t), u_k(t) \rangle \, dt \;+\; \int_0^T \langle A(t)(u_k(t - k), u_k(t)), u_k(t) \rangle \, dt \;=\; \int_0^T \langle f_k(t), u_k(t) \rangle \, dt. \tag{A.29}$$

We use the following transformation

$$\int_0^T \langle w_k'(t), u_k(t) \rangle \, dt = \int_0^T \langle w_k'(t), w_k(t) \rangle \, dt + \int_0^T \langle w_k'(t), u_k(t) - w_k(t) \rangle \, dt$$
$$= \frac{1}{2} \|u^N\|_\Omega^2 - \frac{1}{2} \|u_0\|_\Omega^2 - \frac{1}{2} \sum_{m=1}^N \|u^m - u^{m-1}\|_\Omega^2. \tag{A.30}$$

Eqs. (A.29) and (A.30) together lead to

$$\int_0^T \langle A(t)(u_k(t-k), u_k(t)), u_k(t) \rangle \, \mathrm{d}t$$

$$= \int_0^T \langle f_k(t), u_k(t) \rangle \, \mathrm{d}t - \frac{1}{2} \|u^N\|_\Omega^2 + \frac{1}{2} \|u_0\|_\Omega^2 + \frac{1}{2} \sum_{m=1}^N \|u^m - u^{m-1}\|_\Omega^2. \quad \text{(A.31)}$$

Using Eq. (A.8b), we conclude that the sum in (A.30) and (A.31) is convergent. From Eq. (A.27) we deduce that

$$0 \leqslant \int_0^T \langle f_k(t), u_k(t) \rangle \, \mathrm{d}t + \frac{1}{2} \|u_0\|_\Omega^2 - \frac{1}{2} \|u^N\|_\Omega^2$$

$$+ \frac{1}{2} \sum_{m=1}^N \|u^m - u^{m-1}\|_\Omega^2 - \int_0^T \langle A(t)(u_k(t-k), u_k(t)), v(t) \rangle \, \mathrm{d}t$$

$$- \int_0^T \langle A(t)(u_k(t-k), v(t)), u_k(t) - v(t) \rangle \, \mathrm{d}t. \quad \text{(A.32)}$$

The limit superior in (A.32) leads to

$$0 \leqslant \int_0^T \langle f(t), u(t) \rangle \, \mathrm{d}t + \frac{1}{2} \|u_0\|_\Omega^2 - \frac{1}{2} \|u(T)\|_\Omega^2 + \gamma$$

$$- \int_0^T \langle \zeta(t), v(t) \rangle \, \mathrm{d}t - \int_0^T \langle A(t)(u(t), v(t)), u(t) - v(t) \rangle \, \mathrm{d}t \quad \text{(A.33)}$$

where we used

$$\liminf_{N \to \infty} \|u^N\|_\Omega^2 \geqslant \|u(T)\|_\Omega^2 \quad \text{(A.34)}$$

and

$$u_k(\cdot - k) \to u \quad \text{in } L^2(S, L^2(\Omega)) = L^2(S \times \Omega). \quad \text{(A.35)}$$

This last result follows from Eq. (A.19), the Lebesgue integration theory, and an application of the Nemyzki operator. Eqs. (A.33) and (A.28) lead to

$$-\gamma \leqslant \int_0^T \langle \zeta(t) - A(t)(u(t), v(t)), u(t) - v(t) \rangle \, \mathrm{d}t \quad \forall v \in \mathscr{V}. \quad \text{(A.36)}$$

Now we consider two cases:

(a) If the integral on the right-hand side of (A.36) is always greater or equal to 0, then let $v = u - \alpha w$ with $\alpha > 0$ and $w \in \mathscr{V}$. It follows that

$$0 \leqslant \int_0^T \langle \zeta(t) - A(t)(u(t), u(t) - \alpha w(t)), w(t) \rangle \, \mathrm{d}t \quad \forall w \in \mathscr{V}. \quad \text{(A.37)}$$

Using condition (4.10b), the limit passage for $\alpha \to 0$ is admissible and we obtain

$$0 \leqslant \int_0^T \langle \zeta(t) - A(t)(u(t), u(t)), w(t) \rangle \, \mathrm{d}t \quad \forall w \in \mathscr{V}, \quad \text{(A.38)}$$

and with the standard linearity argument the proof is complete.

(b) If on the other hand the right-hand side of Eq. (A.36) becomes negative, then there exists a $v \in \mathscr{V}$ and (because of continuity) a whole ball $B_r(v) \subset \mathscr{V}$ such that

$$\int_0^T \langle \zeta(t) - A(t)(u(t), v(t)), u(t) - v(t) \rangle \, dt \leqslant 0 \quad \forall v \in B_r(v). \tag{A.39}$$

We set $v = u - w$ with $w \in B_r(u - v)$, and use Eq. (A.39) and the linearity condition (4.10b) to obtain

$$\int_0^T \langle \zeta(t) - A(t)(u(t), u(t) - w(t)), w(t) \rangle \, dt = \int_0^T \langle \zeta(t) - A(t)(u(t), u(t)), w(t) \rangle \, dt$$
$$+ \int_0^T \langle A(t)(u(t), w(t)), w(t) \rangle \, dt \leqslant 0. \tag{A.40}$$

With Eq. (4.7c) we deduce

$$\int_0^T \langle \zeta(t) - A(t)(u(t), u(t)), w(t) \rangle \, dt \leqslant 0 \quad \forall w \in B_r(u - v), \tag{A.41}$$

which yields

$$\int_0^T \langle \zeta(t) - A(t)(u(t), u(t)), \alpha w(t) \rangle \, dt \leqslant 0 \quad \forall \alpha \geqslant 0 \quad \forall w \in B_r(u - v). \tag{A.42}$$

As a result, Eq. (A.41) holds for all $w \in \mathscr{V}$ and using the standard trick of linearity, statement (A.26) is proven.

$$\square$$

A.2 *Proof of a priori estimates*

LEMMA 4.2 There exists a constant C_1, independent of ε, such that the solution Θ_ε of (4.4) (equivalently, $E_{1,\varepsilon}$ and $E_{2,\varepsilon}$ of (4.3)) satisfies

$$\|\Theta_\varepsilon\|_\Omega^2 + \|\kappa_\varepsilon \nabla \Theta_\varepsilon\|_{\Omega,t}^2 = \|E_{1,\varepsilon}\|_{\Omega_\varepsilon^1}^2 + \|\nabla E_{1,\varepsilon}\|_{\Omega_\varepsilon^1,t}^2 + \|E_{2,\varepsilon}\|_{\Omega_\varepsilon^2}^2 + \varepsilon^2 \|\nabla E_{2,\varepsilon}\|_{\Omega_\varepsilon^2,t}^2 \leqslant C_1.$$

Proof. Begin by testing Eq. (4.5) with ρ_ε to obtain

$$(\partial_t \rho_\varepsilon, \rho_\varepsilon)_\Omega + (\kappa_\varepsilon D\omega'(\rho_\varepsilon + \omega^{-1}(T_a))\nabla \rho_\varepsilon, \nabla \rho_\varepsilon)_\Omega = (-\partial_t \omega^{-1}(T_a), \rho_\varepsilon)_\Omega.$$

Because $D\omega'$ is bounded from below by a positive constant, we can apply the definition of κ_ε to get

$$(\partial_t \rho_\varepsilon, \rho_\varepsilon)_\Omega + \min\{D\omega'\}\|\nabla \rho_\varepsilon\|_{\Omega_\varepsilon^1}^2 + \min\{D\omega'\}\|\varepsilon \nabla \rho_\varepsilon\|_{\Omega_\varepsilon^2}^2 \leqslant \|\partial_t \omega^{-1}(T_a)\|_\Omega^2 + \|\rho_\varepsilon\|_\Omega^2.$$

Then, integrating with respect to time and using the boundedness of $\|\omega^{-1}(T_a)\|_\Omega^2$, we conclude using Gronwall's Lemma that

$$\frac{1}{2}\|\rho_\varepsilon(t)\|_\Omega^2 + \min\{D\omega'\}\|\nabla \rho_\varepsilon\|_{\Omega_\varepsilon^1,t}^2 + \min\{D\omega'\}\|\varepsilon \nabla \rho_\varepsilon\|_{\Omega_\varepsilon^2,t}^2 \leqslant C + \frac{1}{2}\|\rho_\varepsilon(0)\|_\Omega^2$$

for every $t \in [0, t_{\mathrm{m}}]$, where we use that the initial conditions are bounded. This yields for Θ_ε that

$$\frac{1}{2}\|\Theta_\varepsilon(t) + \omega^{-1}(T_{\mathrm{a}}(t))\|_\Omega^2 + \min\{D\omega'\}\|\nabla\Theta_\varepsilon\|_{\Omega_\varepsilon^1, t}^2 + \min\{D\omega'\}\|\varepsilon\nabla\Theta_\varepsilon\|_{\Omega_\varepsilon^2, t}^2$$
$$\leqslant C + \frac{1}{2}\|\Theta_\varepsilon(0) + \omega^{-1}(T_{\mathrm{a}}(0))\|_\Omega^2,$$

after which we obtain from the reverse triangle inequality that

$$\frac{1}{2}\|\Theta_\varepsilon(t)\|_\Omega^2 + \min\{D\omega'\}\|\nabla\Theta_\varepsilon\|_{\Omega_\varepsilon^1, t}^2 + \min\{D\omega'\}\|\varepsilon\nabla\Theta_\varepsilon\|_{\Omega_\varepsilon^2, t}^2$$
$$\leqslant C + \frac{1}{2}\|\Theta_\varepsilon(0) + \omega^{-1}(T_{\mathrm{a}}(0))\|_\Omega^2 + \frac{1}{2}\|\omega^{-1}(T_{\mathrm{a}}(t))\|_\Omega^2.$$

This implies for $E_{1,\varepsilon}$ and $E_{2,\varepsilon}$ that

$$\|E_{1,\varepsilon}(t)\|_{\Omega_\varepsilon^1}^2 + \|E_{2,\varepsilon}(t)\|_{\Omega_\varepsilon^2}^2 + \min\{D\omega'\}\|\nabla E_{1,\varepsilon}\|_{\Omega_\varepsilon^1, t}^2 + \min\{D\omega'\}\|\varepsilon\nabla E_{2,\varepsilon}\|_{\Omega_\varepsilon^2, t}^2 \leqslant C_1,$$

where C_1 is a constant independent of ε.   □

A.3 *Proof of uniqueness theorem*

THEOREM 4.2 Equations (4.18) have at most one solution given by

$$T_1 \in \mathscr{V}^1(\Omega) + T_{\mathrm{a}} \quad = \left(L^2\left([0, t_{\mathrm{m}}], \mathscr{H}_0^1(\Omega)\right) + T_{\mathrm{a}}\right) \cap \mathscr{H}^1\left([0, t_{\mathrm{m}}], L^2(\Omega)\right),$$
$$T_2 \in \mathscr{V}^2(\Omega \times Y^2) + T_1 = \left(L^2\left([0, t_{\mathrm{m}}], L^2(\Omega, \mathscr{H}_0^1(Y^2))\right) + T_1\right) \cap \mathscr{H}^1\left([0, t_{\mathrm{m}}], L^2(\Omega \times Y^2)\right),$$

where $T_1 = \omega(E_1)$ and $T_2 = \omega(E_2)$.

Proof. First we note that the cell problem (4.13) has a unique solution, which was proven in Hornung (1997). Hence, we will only prove uniqueness of the macroscopic problem by assuming that there are two solutions $(E_{1,a}, E_{2,a})$ and $(E_{1,b}, E_{2,b})$, and then showing that they are equal. To show uniqueness of solutions to (4.18), we use the equivalent version (4.16) with nonlinear diffusion coefficient. We start by substituting each of our solutions into (4.16), subtract the two equations, and then test with the functions $E_{1,a} - E_{1,b}$ and $E_{2,a} - E_{2,b}$:

$$|Y^1|(\partial_t E_{1,a} - \partial_t E_{1,b}, \, E_{1,a} - E_{1,b})_\Omega$$
$$+ (\Pi(D\omega'(E_{1,a})\nabla E_{1,a} - D\omega'(E_{1,b})\nabla E_{1,b}), \, \nabla E_{1,a} - \nabla E_{1,b})_\Omega$$
$$+ (\partial_t E_{2,a} - \partial_t E_{2,b}, \, E_{2,a} - E_{2,b})_{\Omega \times Y^2}$$
$$+ (D\omega'(E_{2,a})\nabla_y E_{2,a} - D\omega'(E_{2,b})\nabla_y E_{2,b}, \, \nabla_y E_{2,a} - \nabla_y E_{2,b})_{\Omega \times Y^2} = 0.$$

By adding and subtracting an extra term we obtain

$$0 = |Y^1|(\partial_t E_{1,a} - \partial_t E_{1,b}, \, E_{1,a} - E_{1,b})_\Omega$$
$$+ (\Pi(D\omega'(E_{1,a})\nabla E_{1,a} - D\omega'(E_{1,a})\nabla E_{1,b} + D\omega'(E_{1,a})\nabla E_{1,b} - D\omega'(E_{1,b})\nabla E_{1,b}),$$
$$\nabla E_{1,a} - \nabla E_{1,b})_\Omega + (\partial_t E_{2,a} - \partial_t E_{2,b}, \, E_{2,a} - E_{2,b})_{\Omega \times Y^2}$$
$$+ (D\omega'(E_{2,a})\nabla_y E_{2,a} - D\omega'(E_{2,a})\nabla_y E_{2,b} + D\omega'(E_{2,a})\nabla_y E_{2,b} - D\omega'(E_{2,b})\nabla_y E_{2,b},$$
$$\nabla_y E_{2,a} - \nabla_y E_{2,b})_{\Omega \times Y^2},$$

which yields the following estimates

$$
\begin{aligned}
|Y^1|(\partial_t E_{1,a} - \partial_t E_{1,b}, E_{1,a} - E_{1,b})_\Omega &+ \min\{\|\Pi D\omega'\|\}\|\nabla E_{1,a} - \nabla E_{1,b}\|_\Omega^2 \\
&+ (\partial_t E_{2,a} - \partial_t E_{2,b}, E_{2,a} - E_{2,b})_{\Omega \times Y^2} + \min\{D\omega'\}\|\nabla_y E_{2,a} - \nabla E_{2,b}\|_{\Omega \times Y^2}^2 \\
\leqslant &-((D\omega'(E_{1,a}) - D\omega'(E_{1,b}))\nabla E_{1,b}, \nabla E_{1,a} - \nabla E_{1,b})_\Omega \\
&-((D\omega'(E_{2,a}) - D\omega'(E_{2,b}))\nabla_y E_{2,b}, \nabla_y E_{2,a} - \nabla_y E_{2,b})_{\Omega \times Y^2} \\
\leqslant &\|D\omega'(E_{1,a}) - D\omega'(E_{1,b})\|_{L^\infty(\Omega)}\|\nabla E_{1,b}\|_\Omega\|\nabla E_{1,a} - \nabla E_{1,b}\|_\Omega \\
&+ \|D\omega'(E_{2,a}) - D\omega'(E_{2,b})\|_{L^\infty(\Omega \times Y^2)}\|\nabla_y E_{2,b}\|_{\Omega \times Y^2}\|\nabla_y E_{2,a} - \nabla_y E_{2,b}\|_{\Omega \times Y^2}, \\
\leqslant &C_L\|D\omega'(E_{1,a}) - D\omega'(E_{1,b})\|_\Omega\|\nabla E_{1,b}\|_\Omega\|\nabla E_{1,a} - \nabla E_{1,b}\|_\Omega \\
&+ C_L\|D\omega'(E_{2,a}) - D\omega'(E_{2,b})\|_{\Omega \times Y^2}\|\nabla_y E_{2,b}\|_{\Omega \times Y^2}\|\nabla_y E_{2,a} - \nabla_y E_{2,b}\|_{\Omega \times Y^2}, \\
\leqslant &C_D C_L\|E_{1,a} - E_{1,b}\|_\Omega\|\nabla E_{1,b}\|_\Omega\|\nabla E_{1,a} - \nabla E_{1,b}\|_\Omega \\
&+ C_D C_L\|E_{2,a} - E_{2,b}\|_{\Omega \times Y^2}\|\nabla_y E_{2,b}\|_{\Omega \times Y^2}\|\nabla_y E_{2,a} - \nabla_y E_{2,b}\|_{\Omega \times Y^2},
\end{aligned}
$$

Here, we first use Hölder's inequality; secondly that $D\omega'$ is bounded and greater than zero, and Ω is bounded which implies that $\|D\omega(\cdot)\|_{L^\infty(\Omega)} \leqslant C_L\|D\omega(\cdot)\|_\Omega$ for a constant $C_L > 0$; and thirdly we use that $D\omega'$ is Lipschitz continuous with constant C_D. Next, we apply the quadratic formula and integrate with respect to time to get

$$
\begin{aligned}
\frac{1}{2}|Y^1|\|\|E_{1,a} - E_{1,b}\|_\Omega^2 &+ \min\{\|\Pi D\omega'\|\}\|\nabla E_{1,a} - \nabla E_{1,b}\|_{\Omega,t}^2 \\
&+ \frac{1}{2}\|E_{2,a} - E_{2,b}\|_{\Omega \times Y^2}^2 + \min\{D\omega'\}\|\nabla_y E_{2,a} - \nabla E_{2,b}\|_{\Omega \times Y^2,t}^2 \\
\leqslant &\frac{C_D C_L \lambda}{2}\int_0^{t_m}\|E_{1,a} - E_{1,b}\|_\Omega^2\|\nabla E_{1,b}\|_\Omega^2\,\mathrm{d}t + \frac{C_D C_L}{2\lambda}\|\nabla E_{1,a} - \nabla E_{1,b}\|_{\Omega,t}^2 \\
&+ \frac{C_D C_L \lambda}{2}\int_0^{t_m}\|E_{2,a} - E_{2,b}\|_{\Omega \times Y^2}^2\|\nabla_y E_{2,b}\|_{\Omega \times Y^2}^2\,\mathrm{d}t + \frac{C_D C_L}{2\lambda}\|\nabla_y E_{2,a} - \nabla_y E_{2,b}\|_{\Omega \times Y^2,t}^2,
\end{aligned}
$$

for any $\lambda > 0$, where we have taken advantage of the fact that terms containing the initial conditions are zero. Rearranging terms yields

$$
\begin{aligned}
\frac{1}{2}|Y^1|\|\|E_{1,a} - E_{1,b}\|_\Omega^2 &+ \left(\min\{\|\Pi D\omega'\|\} - \frac{C_D C_L}{2\lambda}\right)\|\nabla E_{1,a} - \nabla E_{1,b}\|_{\Omega,t}^2 \\
&+ \frac{1}{2}\|E_{2,a} - E_{2,b}\|_{\Omega \times Y^2}^2 + \left(\min\{D\omega'\} - \frac{C_D C_L}{2\lambda}\right)\|\nabla_y E_{2,a} - \nabla E_{2,b}\|_{\Omega \times Y^2,t}^2 \\
\leqslant &\frac{C_D C_L \lambda}{2}\int_0^{t_m}\|E_{1,a} - E_{1,b}\|_\Omega^2\|\nabla E_{1,b}\|_\Omega^2\,\mathrm{d}t + \frac{C_D C_L \lambda}{2}\int_0^{t_m}\|E_{2,a} - E_{2,b}\|_{\Omega \times Y^2}^2\|\nabla_y E_{2,b}\|_{\Omega \times Y^2}^2\,\mathrm{d}t.
\end{aligned}
$$

Finally, we choose λ large enough such that all terms on the left-hand side are positive and exploit that $\|\nabla E_1\|_\Omega^2$ and $\|\nabla_y E_2\|_\Omega^2$ are bounded, after which we can apply Gronwall's Lemma to obtain

$$
\|E_{1,a} - E_{1,b}\|_\Omega^2 + \|\nabla E_{1,a} - \nabla E_{1,b}\|_{\Omega,t}^2 + \|E_{2,a} - E_{2,b}\|_{\Omega \times Y^2}^2 + \|\nabla_y E_{2,a} - \nabla E_{2,b}\|_{\Omega \times Y^2,t}^2 \leqslant 0.
$$

Consequently, $E_{1,a} = E_{1,b}$ and $\nabla E_{1,a} = \nabla E_{1,b}$ almost everywhere on $\Omega \times [0, t_m]$, and similarly $E_{2,a} = E_{2,b}$ and $\nabla E_{2,a} = \nabla E_{2,b}$ almost everywhere on $\Omega \times Y^2 \times [0, t_m]$. □

Acknowledgements

REFERENCES

Allaire, G. (1992) Homogenization and two-scale convergence. *SIAM J. Math. Anal.*, **23**(6), 1482–1518.

Améglio, T., Ewers, F. W., Cochard, H., Martignac, M., Vandame, M., Bodet, C. & Cruiziat, P. (2001) Winter stem xylem pressure in walnut trees: Effects of carbohydrates, cooling and freezing. *Tree Physiol.*, **21**, 387–394.

Arbogast, T., Douglas, J. & Hornung, U. (1990) Derivation of the double porosity model of single phase flow via homogenization theory. *SIAM J. Math. Anal.*, **21**, 823–836.

Bossavit, A. & Damlamian, A. (1981) Homogenization of the Stefan problem and application to magnetic composite media. *IMA J. Appl. Math.*, **27**, 319–334.

Brown, S. (2015) Global warming pushes maple trees, syrup to the brink. The Plate, National Geographic Society. Available at `http://theplate.nationalgeographic.com/2015/12/02`.

Ceseri, M. & Stockie, J. M. (2013) A mathematical model of sap exudation in maple trees governed by ice melting, gas dissolution and osmosis. *SIAM J. Appl. Math.*, **73**(2), 649–676.

Chavarría-Krauser, A. & Ptashnyk, M. (2010) Homogenization of long-range auxin transport in plant tissues. *Nonlin. Anal. Real World Applic.*, **11**(4524-4532).

Chavarría-Krauser, A. & Ptashnyk, M. (2013) Homogenization approach to water transport in plant tissues with periodic microstructures. *Math. Model. Nat. Phenom.*, **8**(4), 80–111.

Cioranescu, D. & Donato, P. (1999) *An Introduction to Homogenization*. Oxford University Press.

Cirelli, D., Jagels, R. & Tyree, M. T. (2008) Towards an improved model of maple sap exudation: The location and role of osmotic barriers in sugar maple, butternut and white birch. *Tree Physiol.*, **28**, 1145–1155.

COMSOL (2015) COMSOL Multiphysics Version 5.0. COMSOL, Inc., Palo Alto, CA.

Damlamian, A. (1981) How to homogenize a nonlinear diffusion equation: Stefan's problem. *SIAM J. Math. Anal.*, **12**(3), 306–313.

Dautray, R. & Lions, J.-L. (2000) *Mathematical Analysis and Numerical Methods for Science and Technology, Volume 5, Evolution Problems I*. Springer-Verlag Berlin Heidelberg.

Eck, C. (2004) Homogenization of a phase field model for binary mixtures. *Multiscale Model. Simul.*, **3**(1), 1–27.

Engquist, B., Lötstedt, P. & Runborg, O., editors (2005) *Multiscale Methods in Science and Engineering*, volume 44 of *Lecture Notes in Computational Science and Engineering*. Springer, Berlin.

Graf, I., Ceseri, M. & Stockie, J. M. (2015) Multiscale model of a freeze–thaw process for tree sap exudation. *J. Roy. Soc. Interface*, **12**, 20150665.

Graf, I. & Peter, M. A. (2014) Homogenization of fast diffusion on surfaces with a two-step method and an application to T-cell signaling. *Nonlin. Anal. Real World Applic.*, **17**, 344–364.

Hornung, U. (1997) *Homogenization and Porous Media*, volume 6 of *Interdisciplinary Applied Mathematics*. Springer, New York.

Johnson, R. W., Tyree, M. T. & Dixon, M. A. (1987) A requirement for sucrose in xylem sap flow from dormant maple trees. *Plant Physiol.*, **84**, 495–500.

Kanschat-Krebs, O. P. (2015) Homogenization and the Stefan Problem. Master's thesis, Angewandte Analysis, Universität Augsburg, Augsburg, Germany.

Kramer, P. J. & Boyer, J. S. (1995) The absorption of water and root and stem pressures. In *Water Relations of Plants and Soils*, chapter 6, pages 167–200. Academic Press, London.

MATLAB (2015) MATLAB Release 2015a. The Mathworks, Inc., Natick, MA.

Milburn, J. A. & Kallarackal, J. (1991) Sap exudation. In Raghavendra, A. S., editor, *Physiology of Trees*, chap-

ter 16, pages 385–402. John Wiley & Sons, New York.

Milburn, J. A. & O'Malley, P. E. R. (1984) Freeze-induced sap absorption in *Acer pseudoplatanus*: A possible mechanism. *Can. J. Bot.*, **62**, 2101–2106.

Nguetseng, G. (1989) A general convergence result for a functional related to the theory of homogenization. *SIAM J. Math. Anal.*, **20**(3), 608–629.

Peter, M. A. (2007a) Homogenisation in domains with evolving microstructure. *C. R. Mécanique*, **335**(7), 357–362.

Peter, M. A. (2007b) Homogenisation of a chemical degradation mechanism inducing an evolving microstructure. *C. R. Mécanique*, **335**(11), 679–684.

Peter, M. A. & Böhm, M. (2008) Different choises of scaling in homogenization of diffusion and interfacial exchange in a porous medium. *Math. Methods Appl. Sci.*, **31**, 1257–1282.

Peter, M. A. & Böhm, M. (2009) Multiscale modelling of chemical degradation mechanisms in porous media with evolving microstructure. *Multiscale Model. Simul.*, **7**(4), 1643–1668.

Tyree, M. T. (1995) The mechanism of maple sap exudation. In Terazawa, M., McLeod, C. A. & Tamai, Y., editors, *Tree Sap: Proceedings of the 1st International Symposium on Sap Utilization*, pages 37–45, Bifuka, Japan. Hokkaido University Press.

Visintin, A. (1996) *Models of Phase Transition*, volume 28 of *Progress in Nonlinear Differential Equations and Their Applications*. Birkhäuser, Boston.

Visintin, A. (2007) Homogenization of a doubly nonlinear Stefan-type problem. *SIAM J. Math. Anal.*, **39**(3), 987–1017.

Wilmot, T. R. (2011) Root pressure in trees: A spring phenomenon. *Farming: Journal of Northeast Agriculture*.

Wolff, M. (2016) Partielle Differentialgleichungen und Sobolev-Räume. Unpublished lecture notes, Zentrum für Technomathematik, Universität Bremen.